EUROPEAN ORGANIZATION FOR NUCLEAR RESEARCH

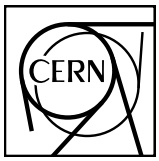

ALICE-PUBLIC-2021-006

Performance of the ALICE HMPID detector during the LHC run period 2010−2015 and perspectives

ALICE Collaboration*

Abstract

In this note the performance of the ALICE High Momentum Particle IDentification (HMPID) detector during the LHC run period 2010−2015 is presented. The HMPID extends the charged hadron identification capability of the ALICE apparatus at high momenta, identifying with three sigma separation power charged pions and kaons in the momentum range 1−3 GeV/c and (anti-)protons in the range 1.5−5 GeV/c. It consists of seven Ring Imaging Cherenkov (RICH) modules, $1.3\times1.32\times0.3$ m^3 each. The detection of Cherenkov UV photons is achieved by Multiwire Proportional Chambers (MWPCs) with CsI pad segmented photocathodes, for a total active area of 10.3 m^2. The Cherenkov radiator used is the liquid C_6F_{14} (perfluorohexane) with $n = 1.299$ at a photon wavelength $\lambda = 175$ nm. The detector stability with emphasis on the CsI quantum efficiency and the Particle IDentification (PID) performance, by means of both statistical and track-by-track approaches, are presented. Finally, the perspective of the detector operation during the Run 3 data-taking period (2022−2024) with Pb−Pb runs at 50 kHz of collision rate, is briefly discussed and evidence for the effective detector operation is provided.

*See Appendix A for the list of collaboration members

1 Introduction

ALICE, A Large Ion Collider Experiment [1, 2] at the CERN LHC, was designed to study the physics of strongly interacting matter at extreme temperatures and energy densities produced in nucleus–nucleus collisions, where the formation of a new phase of matter, the quark–gluon plasma, is expected. The existence of such a phase and its properties are key issues in Quantum Chromodynamic (QCD) for the understanding of quark confinement and chiral-symmetry restoration. To study the QGP properties, ALICE combines different detector techniques allowing Particle IDentification (PID) in a wide transverse momentum (p_{T}) range from hundreds of MeV/c up to about 100 GeV/c.

The HMPID detector [3] can identify charged pions and kaons in the p_{T} range $1-3$ GeV/c and (anti-)protons in the range $1.5-5$ GeV/c. It consists of seven Ring Imaging Cherenkov (RICH) modules, $1.3\times1.32\times0.3$ m^3 each. It covers 5% of the central barrel acceptance in the pseudorapidity interval $|\eta| < 0.6$ and $\Delta\phi \approx 60^\circ$, with a distance from the interaction point is about 5 m. The HMPID enhances the ALICE PID performance enabling identification of charged hadrons beyond the momentum interval achievable in the Inner Tracking System (ITS), Time Projection Chamber (TPC) and Time Of Flight (TOF) detectors.

In 1993 the Research and Development project 26 (RD26) was launched at CERN to explore solutions for particle identification based on RICH counters equipped with large area Cesium Iodine (CsI) photocathodes (PCs) for Multiwire Proportional Chambers (MWPC), less expensive than vacuum photodetectors. The main technological issues were how to get a reliable production process for reproducible CsI quantum efficiency (QE) in several tens of photocathodes (CsI PCs), with a surface up to 0.3 m^2, and how to ensure the QE stability on a time scale of several years, compatible with the duration of high energy physics experiments. The development pursued in the RD26 project was also of interest to the COMPASS [4] and the HADES [5] collaborations.

In 1999 a RICH prototype, 2/3 of the final module size, was installed in the STAR experiment at the Brookhaven National Laboratory (BNL) Relativistic Heavy Ion Collider (RHIC) in the USA. The detector transportation from CERN to USA, its operation over two years and the PID carried out combining the HMPID data with the momentum measured by the STAR Time Projection Chamber, validated the capabilities of a large area CsI-based RICH detector as a PID system at colliders [6–8].

After the experience at BNL, before starting the mass production of the seven RICH modules (2004-2006), dedicated aging tests using radioactive source (^{90}Sr) were carried out at CERN [9–11] to further investigate the stability of the CsI QE, simulating 10 years of operation in ALICE. The charge dose so far accumulated and the expected additional integrated luminosity during the LHC Run 3 data-taking period with Pb$-$Pb runs at 50 kHz of collision rate, will finally result in a CsI charge absorbed dose of about 0.2 mC/cm^2, a value for which no relevant CsI aging effect have been observed

In this note the HMPID performance during the LHC Run 1 data-taking period (2010-2013) and part of Run 2 (2015) are presented. Then two PID approaches, namely statistical and track-by-track, with the relative performances, are presented. Finally, the perspective to operate the HMPID during the Run 3 data-taking period (2022-2024) with Pb$-$Pb runs at 50 kHz, is briefly discussed.

2 The HMPID principle of operation and layout

The HMPID consists of seven RICH modules (RICH0-6), of about $1.3\times1.32\times0.3$ m^3 each, with proximity focusing geometry. The Cherenkov photons emitted by the charged particles traversing the radiator are detected by photon counters made of a 300 nm layer of CsI deposited onto the pad segmented photocathodes of a MWPC filled with pure CH_4. The total CsI active area is 10.3 m^2. Liquid C_6F_{14} (perfluorohexane) is used as Cherenkov radiator, which has a refractive index $n = 1.299$ at $\lambda = 175$ nm where the CsI QE is approximately 25%.

In each RICH module three quartz radiator vessels for the C_6F_{14} with dimensions $1.3\times0.4\times0.025$ m^3 are installed. They are assembled by gluing NEOCERAM plates and fused silica optical windows (transparent to the Cherenkov UV photons). In Fig. 1 the layout of a section of one RICH module is shown. The Cherenkov photons produced in 15 mm of C_6F_{14} propagate through the proximity gap down to the CsI photocathode where they are converted into photoelectrons. The avalanche multiplication in the MWPC induces a charge signal on the pads. The collection electrode is designed to remove electrons produced by the ionization in the proximity gap, it is set to a voltage of 500 V.

A readout electronics digitalizes the photoelectron cluster charge induced on the CsI pad segmented photocathode. This with the module geometry allows for the Cherenkov angle to be determined.

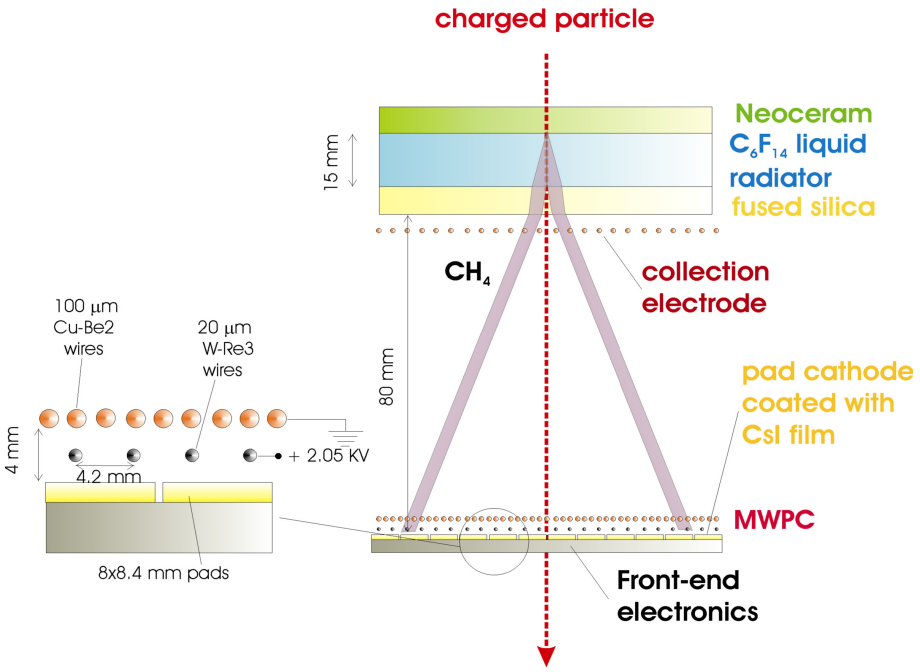

Fig. 1: Layout of a section of one RICH module.

Figure 2 shows the HMPID detector modules on the cradle during its insertion inside the ALICE solenoid on September 2006. They are located in the 1 to 3 o'clock positions.

3 Performance and stability of the HMPID subsystems

In this section, we describe the HMPID sub-systems, namely: the Detector Control System (DCS), the Front End Electronics (FEE) and Read Out (RO) electronics, the Low-Voltage (LV) and High-Voltage (HV) power system, the cooling system, the C_6F_{14} recirculation system (LCS), the MWPC and finally the CsI photocathodes (PCs).

3.1 The Detector Control System

The HMPID DCS [12] ensures remote detector operation, monitoring and archiving. In Fig. 3 the User Interface (UI) of the HMPID DCS is shown. The command execution is based on Finite State Machines (FSM). The FSM architecture and the navigator tree is shown on the left side of the UI whereas on the right side the monitoring panel corresponding to the selected FSM node is shown. Figure 4 shows the segmentation of the different sub-systems in one RICH module as it appears in the DCS: six HV sectors (HVs0-5) of 48 wires each, running over two half PCs; six LV sectors (FEE0-5) and two readout systems (ROL and ROR). The ROL is reading one half of the FEE segments covering PC0, 2, 4, whereas ROR is reading the complementary half segments covering the PC1, 3, 5.

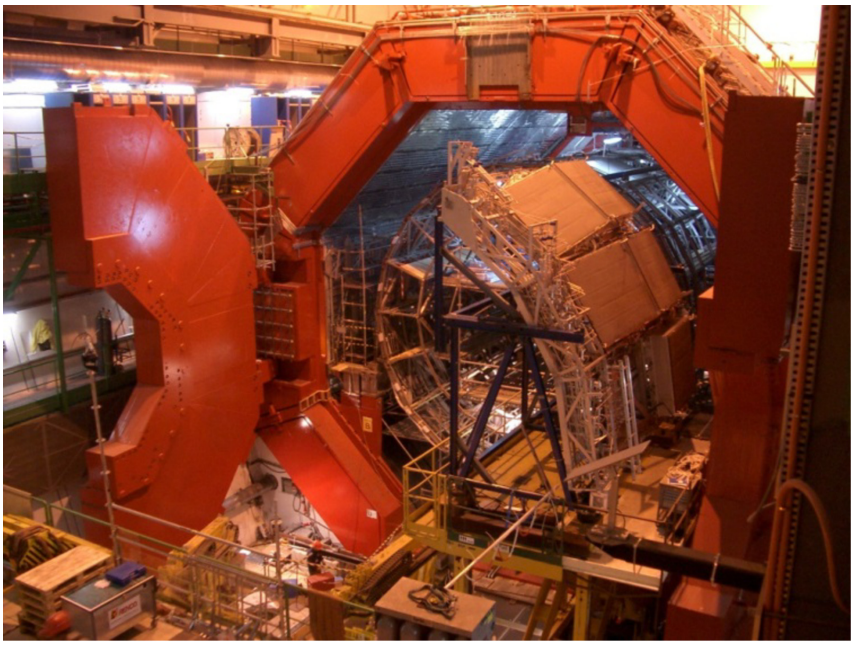

Fig. 2: September 2006: the HMPID cradle with the seven RICH modules was inserted in the ALICE solenoid. It was the first detector installed in the experiment.

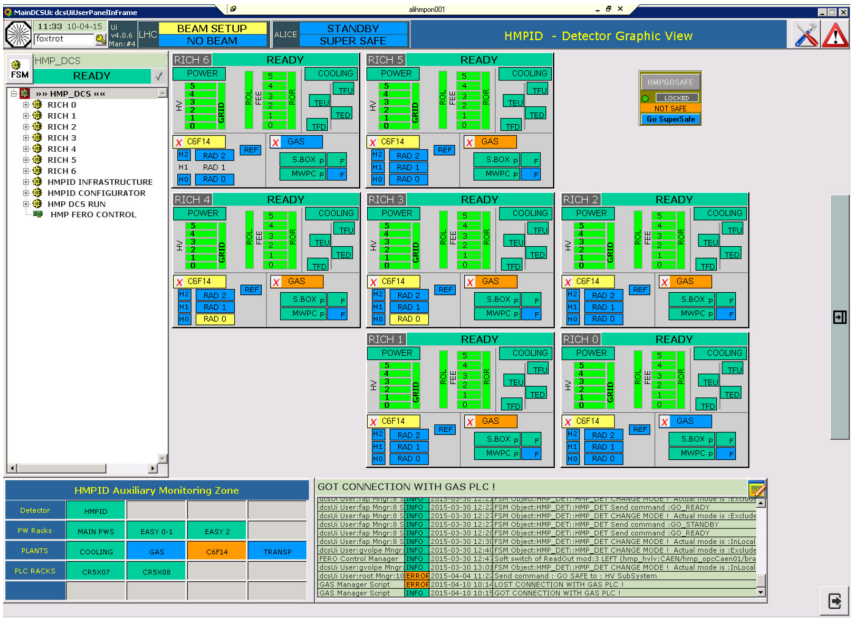

Fig. 3: HMPID DCS User Interface. The Finite State Machine control navigator is located on the left, and the monitoring panel corresponding to the selected FSM node, in this case the HMP-DCS, on the right side.

3.2 Front End and Read Out electronics

The FEE and RO electronics are based on two dedicated ASIC chips: the GASSIPLEX [13, 14] and the DILOGIC [14], respectively. The analogue GASSIPLEX chip is a low-noise signal processor (1000 e^- noise equivalent). The Dilogic-2 circuit was developed to process data produced by a 12 bits Analog to Digital Converter (ADC), with a conversion time of about 20 ns. It subtracts the baseline of the FEE channel (pedestal) and suppresses empty channels (zero suppression), selecting valid data and reducing the size of the stored data. The percentage of FEE dead channels is of the order of 0.15%, and no RO board failures were observed.

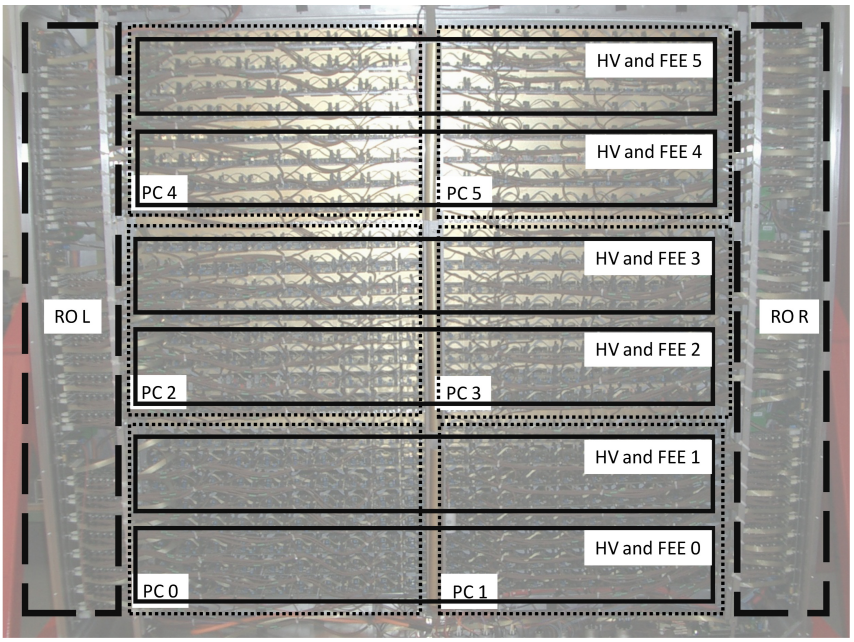

Fig. 4: Correspondence of DCS control units (continuous and dashed line boxes) with the hardware of one RICH module. There are two readout systems, left and right (ROL and ROR), six HV sectors and six LV sectors, marked as FEE. Each HV sector powers two half CsI photocathodes (dotted line boxes).

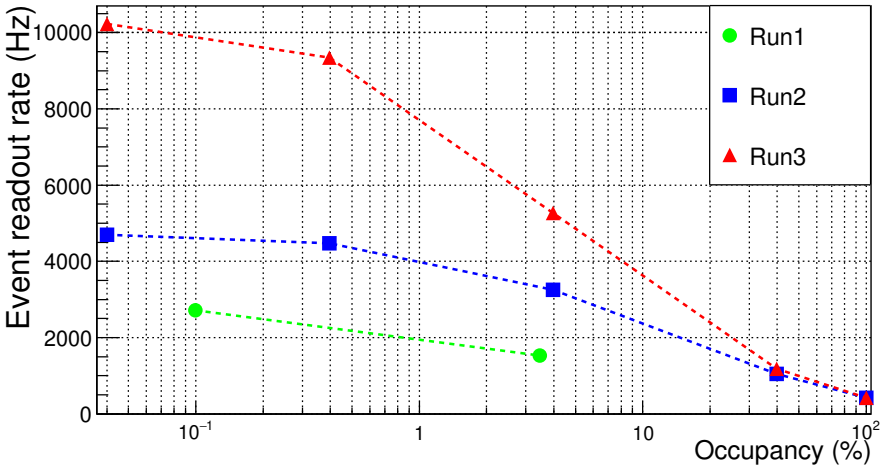

Fig. 5: Event readout rate as a function of the detector occupancy during Run 1, Run 2 and Run 3 data taking periods. The input trigger rate used in the test is 100 kHz.

During the first long shutdown LS1 (2013-2015), a substantial improvement of the readout firmware was carried out. Reinforced protections against overlapping L0 triggers, an improved clock distribution among the software modules in the FPGA (ALTERA Stratix II EP2S15F484C5, installed on the Readout Common Board (RCB) interfacing the FEE communication bus, the DAQ and the Trigger systems), the latching of the detector data bus and the redefinition of the hardware-software reset of the electronics were put in place. As a consequence, the event readout rate in pp collisions ($\approx 0.1\%$ detector occupancy) increased from 2.7 kHz to 4.7 kHz and from 1.5 kHz to 3.0 kHz in central Pb–Pb collisions ($\approx 3\%$ detector occupancy). Also the Common Data Header (CDH) was modified to accommodate 100 trigger classes making the HMPID compliant with the experimental requirements for the Run 2 data-taking period. Moreover, 14 Ethernet-JTAG interfaces for the 14 FPGAs, two for each RICH module (one

for ROL and one for ROR), were installed, providing enhanced flexibility for remote updating of new firmware versions.

During Run 3 the readout in ALICE will be in continuous mode. The data stream will be tagged with the orbit signal (HB Trigger) [15]. The HMPID will remain a triggered detector with only two trigger levels, L0 and L1. The L2 will be removed with a reduction of 100 microseconds of the event processing time, with a corresponding increase of the event readout rate. Preliminary laboratory tests with the HMPID show an increased readout rate up to 10 kHz and 7 kHz in pp and Pb–Pb collisions, respectively. The readout performance in Run 1 (green line) and Run 2 (blue line), and the expected rate in Run 3 as obtained in laboratory tests (red line), are shown in Fig. 5.

3.3 HV and LV system

The HV and LV system is based on the system crate CAEN SY1527. The HV system uses five 12-channel A1821PH boards, specifically developed for the HMPID, with 1 nA current sensitivity. The LV EASY system consists of seven A3009 boards for the FEE sectors and four A3025 boards for the RO electronics. The A3009 is a 12-channel board with 8V-9A/channel max, and the A3025 is a 4-channel board with 8V-25A max.

During the entire 2010−2015 period the HV and LV power system was very stable, only two LV boards out of eleven showed a single channel failure and were replaced.

3.4 Cooling system

The HMPID cooling system was designed to remove about 400 W of dissipated power from the FEE and RO electronics. In Fig. 6 a schematic view of the cooling system is shown. The cooling water circulates in the panels used to close the aluminum protection boxes to shield and protect the FEE and RO electronics. To prevent water condensation on the electronics, the protection box is flushed with N_2.

The temperature monitoring in each RICH module is done by means of four PT100 sensors installed in the protection box: two are fixed to the MWPC aluminum frame (one sensor at the top and the other at the bottom), and two in the protection box to probe the temperature of the N_2 gas.

The temperature gradient measured on the aluminum frame is on average 6 °C ($\approx$ 24 °C at the bottom sensor and $\approx$ 30 °C at the top sensor). This is caused by the different N_2 density in the protection box in contact with the MWPC aluminium frame. The almost vertical position of the RICH modules explains the warmer zone in the top part of the module.. The same temperature profile is present in the radiator vessels as well (see paragraph 3.5.1) and it is used to calculate offline the actual C_6F_{14} refractive index. To maximize the cooling efficiency, slabs of insulating foam are glued on the external side of the cooling panels.

3.5 Liquid circulation system

The liquid circulation system (LCS) provides both circulation and filtering of the liquid C_6F_{14} to ensure its best transparency to the emitted UV Cherenkov photons. It is composed of three parts: the pumping station, the distribution station and the filling and purifying station. A dedicated system provides regular measurements of the C_6F_{14} transparency, which was stable in the period 2010-2015. In Fig. 7, as an example, four months of measurements during 2015, are shown. The observed 2% of increase is not relevant if propagated on the $N_{\rm ph}$ detected that is of the order of 12. Therefore it has no impact on the physics performance.

The C_6F_{14}, a chemically inert, non-aromatic saturated fluorocarbon, was chosen as Cherenkov radiator primarily because of its optical properties. With the refractive index $n = 1.299$ at 175 nm that corresponds to a β threshold for the Cherenkov emission of $\beta_{th} = 0.77$, it is suitable for the PID in the required

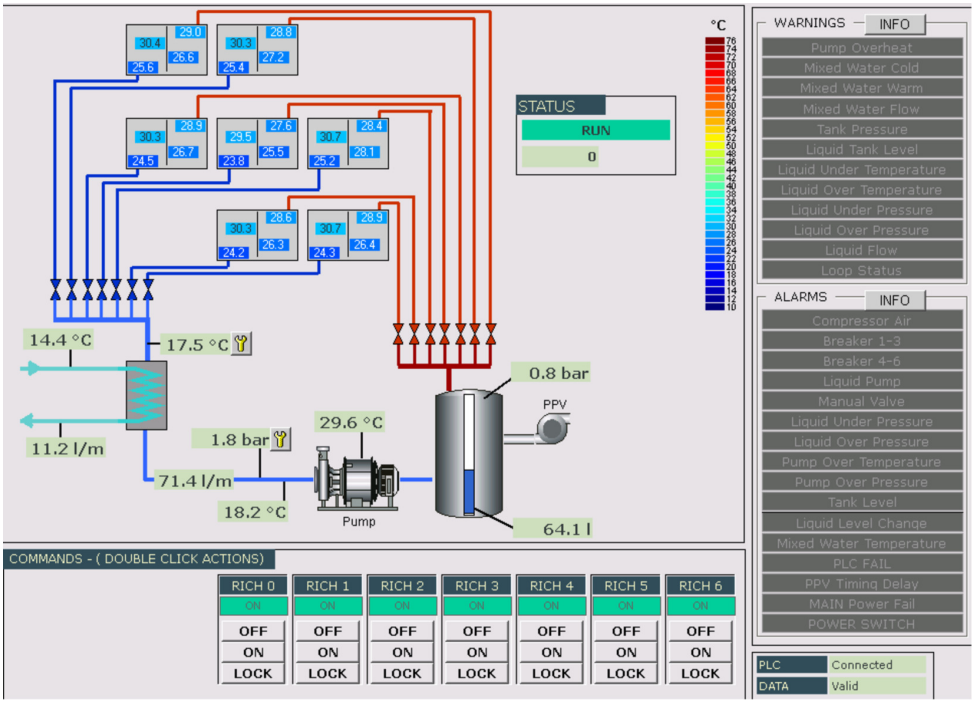

Fig. 6: Schematic view of the cooling system taken from the DCS User Interface. The loop control buttons and the location in the protection box of the four PT100 sensors are shown.

momentum interval. The circulation through the radiator vessels is based on a gravity flow mechanism to prevent accidental overpressure. Each vessel is fed by a so called header tube where an overflow is set to establish the correct hydrostatic pressure.

The C_6F_{14} low boiling point (51 °C) results in an elevated vapor pressure, approximately 310 mbar at 25 °C. To minimize the losses by evaporation, during the Run 1 data-taking period the liquid was circulated and purified only during the Pb–Pb data taking period while it was stagnant during pp periods and the LHC technical stops. In both conditions, no evident transparency differences were measured showing that the liquid radiator was affected by low levels of contaminants.

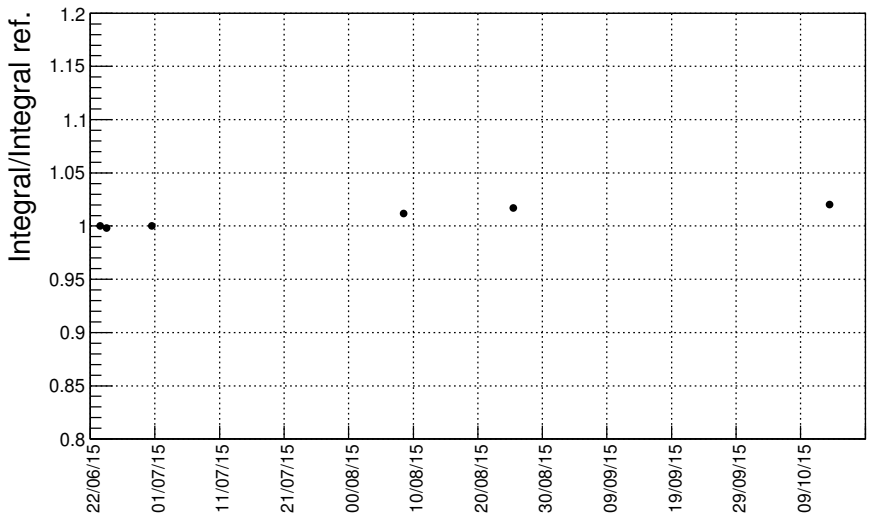

Fig. 7: Ratio of the integral over the wavelength of the transparency distribution to a reference value.

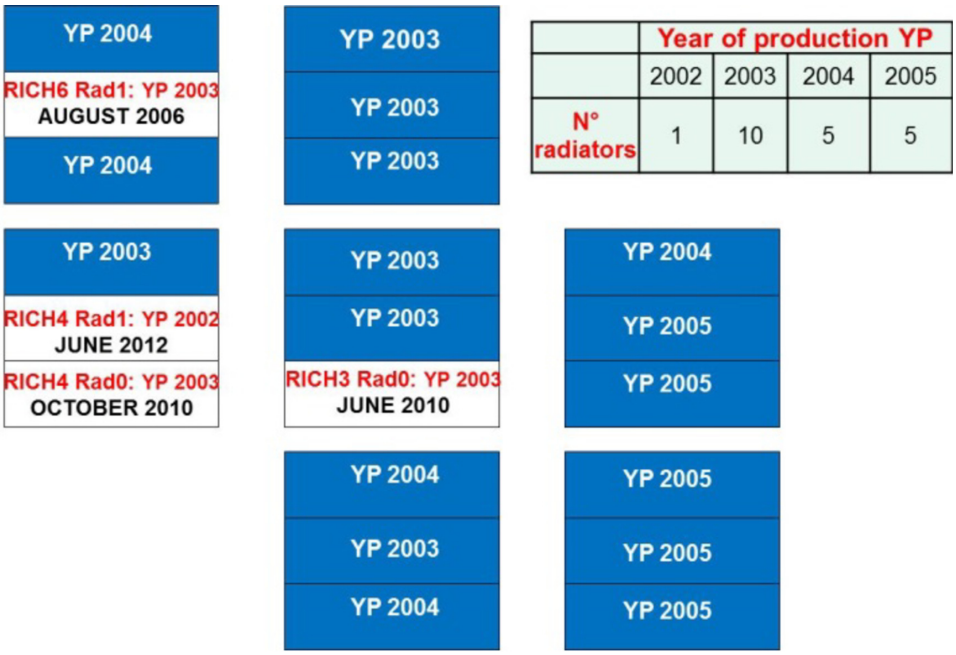

	Year of production YP			
	2002	2003	2004	2005
N° radiators	1	10	5	5

Fig. 8: Layout of the radiator vessels with the year of production. The white boxes represent the radiator vessels that were leaking at the end of Run 1. The interaction point is behind the figure plane.

3.5.1 Construction and stability of the quartz radiator vessels for the C_6F_{14}

Each RICH module is equipped with three radiator vessels, each one covering the acceptance of two CsI PCs, a detailed description can be found in Ref. [3]. A radiator tray consists of one NEOCERAM plate of $1330\times413\times4$ mm^3, three UV grade fused silica plates of $443\times413\times5$ mm^3 transparent to the UV Cherenkov photons, four NEOCERAM side bars, 15 mm high, and 30 cylindrical quartz spacers, 10 mm in diameter and 15 mm high. The resulting surface and thickness of the liquid C_6F_{14} contained in the tray are $1330\times413\times15$ mm^3.

All the elements were glued using ARALDITE 2011 supplied by VANTICO. This denomination appeared in 2003 as this glue was formerly known as AW 106. In order to ensure the long-term tightness of the vessels, the machining, polishing and gluing procedure of the NEOCERAM and quartz plates were established and carefully followed during the vessel assembly. In particular, the design and construction of the vessels was based on the experience gained in RICH systems of other experiments (DELPHI and SLD), equipped with similar radiator trays, and on compatibility of all selected materials with the usage of the C_6F_{14} [16].

All the trays were tested before their installation in the RICH modules. In Fig. 8, their layout and the year of production (YP) are shown. The interaction point is located behind the figure plane. In Fig. 8 the white boxes represent the position of the four (out of 42) radiator vessels that started to leak during Run 1. In black the date when the leak started is indicated. So far the exact reason of the leakages is not know, we can just formulate some hypothesis (detector ageing). The broken radiator vessels was emptied and isolated.

3.6 Multi-Wire Proportional Chamber (MWPC)

3.6.1 Geometry and stability of MWPC

Details on the MWPC design and construction are given in [3]. We summarise some basic features here. The MWPC has asymmetric gaps, the anode wire-CsI photocathode gap is 2 mm, whereas the anode wire-cathode wire gap is 2.4 mm. Such an asymmetry optimizes the coupling between anode wires and

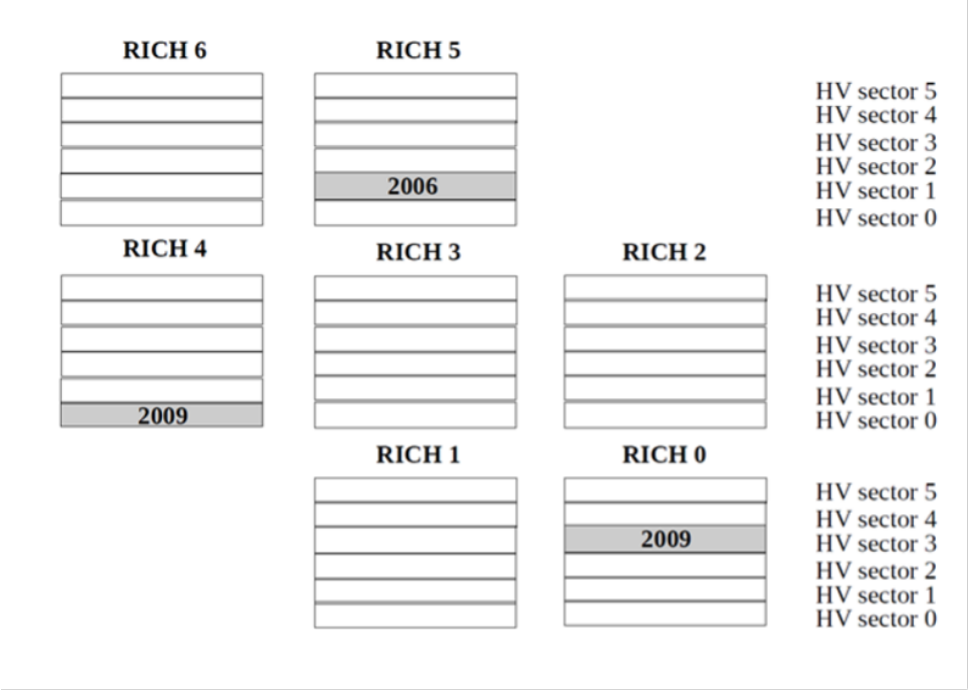

Fig. 9: Map of the excluded HV sectors and the year when they have been excluded.

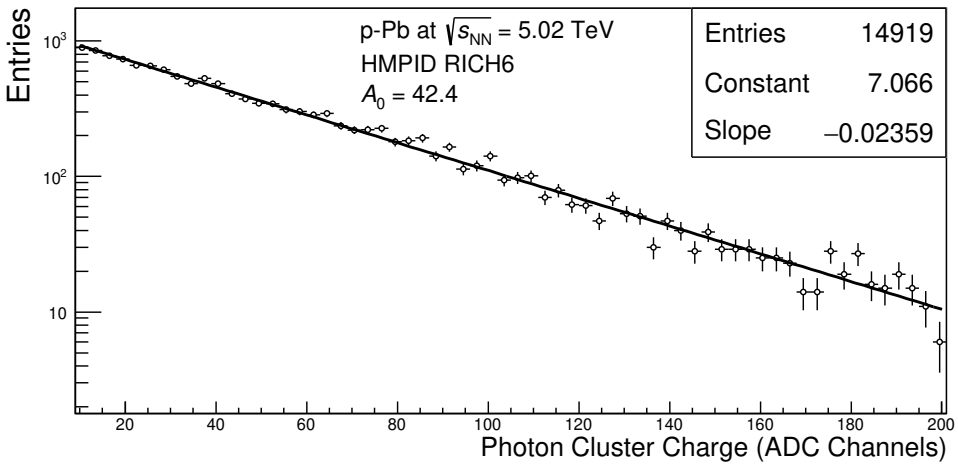

Fig. 10: Example of Single Electron Pulse Height Distribution (SEPHD) in RICH6 HV sector 5, extracted from p–Pb collisions at $\sqrt{s_{NN}}$ = 5.02 TeV data, collected in 2013. A_0 is the inverse of the slope of the fit.

pad cathode plane. The 20 μm anode wires have a 4.2 mm pitch and are soldered, whereas the 100 μm cathode and collecting grid wires, with a pitch of 2 mm, are crimped. To remove electrons produced by the ionizing track from the proximity gap, a collecting grid is located close to the radiator vessels and biased with 400 V. A voltage of about 2050 V is needed to obtain a visible gas gain of about 4×10^4 at the FEE integration time of about 1 μs, with respect to a total gain of $\approx 8\times10^4$ at the ion drift time (>10 μsec).

As shown in Fig. 4, each MWPC is powered by six HV sectors. Few HV sectors due to discharges were excluded and set to a lower voltage than the working one. Figure 9 shows the position of the excluded HV sectors as gray boxes within the HMPID layout. The year of the exclusion is also indicated. Considering only the excluded HV sectors, the detector acceptance reduces to $\approx 90\%$. Considering also the excluded

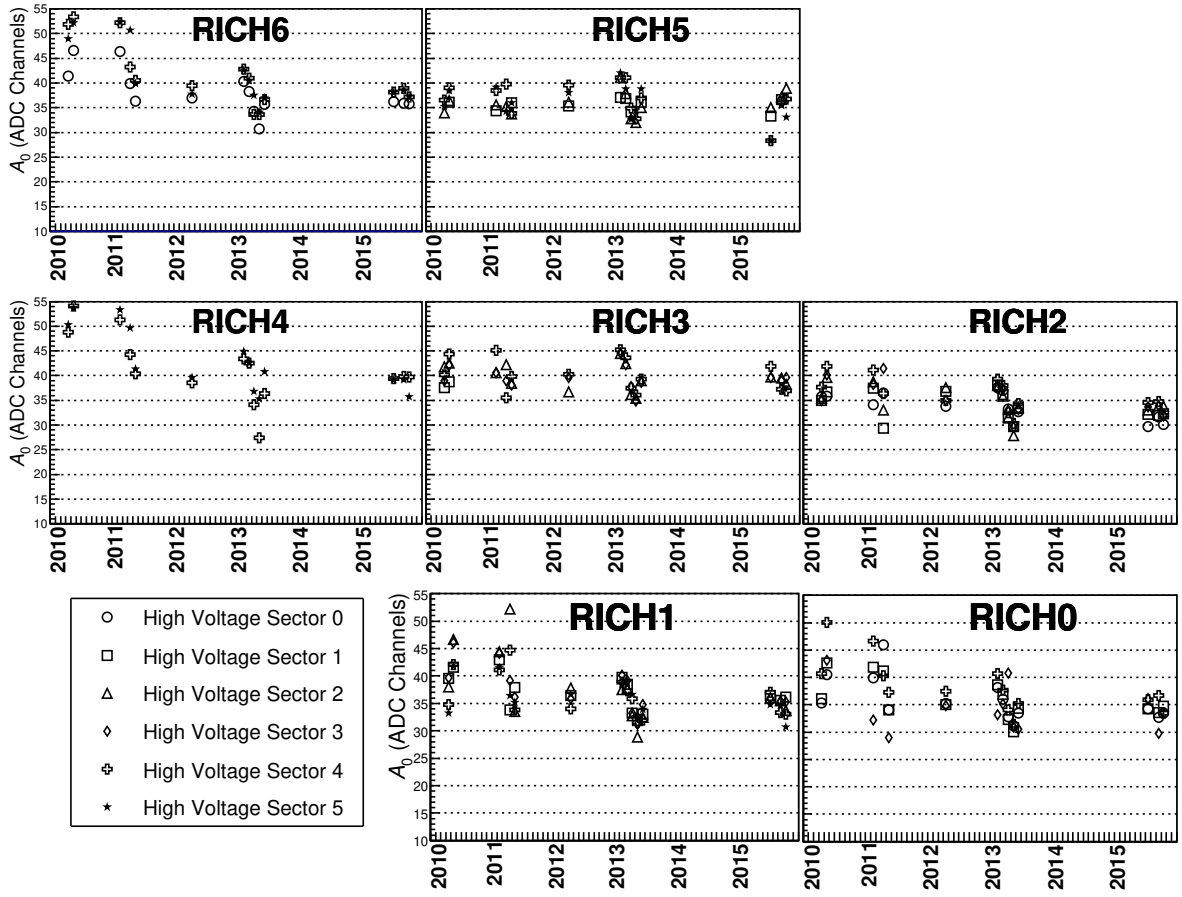

Fig. 11: A_0 parameters as a function of time for the various HV sectors. A_0 is related to the chamber gain.

leaking trays, the detector acceptance reduces to $\approx 70\%$ with a good stability after more than ten years from the construction.

3.6.2 CH_4 gas gain stability and uniformity

A stable gas gain at the design value of about 4×10^4 minimizes the impact of the ion bombardment on the CsI ensuring an efficiency of about 90% for single photoelectron detection. The single photoelectron detection efficiency is defined as follows:

$$\varepsilon_{\text{det}} = \mathrm{e}^{-\frac{A_{\text{th}}}{A_0}} \tag{1}$$

where A_0 is the average single electron pulse height and A_{th} is the detection threshold for the FEE electronics. The gain monitoring was performed by measuring the Single Electron Pulse Height Distributions (SEPHD). Figure 10 shows an example of the SEPHD in the RICH6 HV sector 5. The A_0 parameter extracted from an exponential fit to the SEPHDs for each HV sector and for the various ALICE data taking periods is shown in Fig. 11, where each group of narrowly spaced points refers to the same period. The vertical spread of measurements for the same data taking period is due to the different gain among the six HV sectors in the MWPC. In fact, on average, due to the temperature gradient, the gain increases going from the bottom to the top of the chamber, as can be observed in Fig. 12 (empty circles) for each module (RICH0-6 correspond to ch0-6 in the figure).

In September 2011 the gain spread among the different HV sectors was reduced by a HV equalization

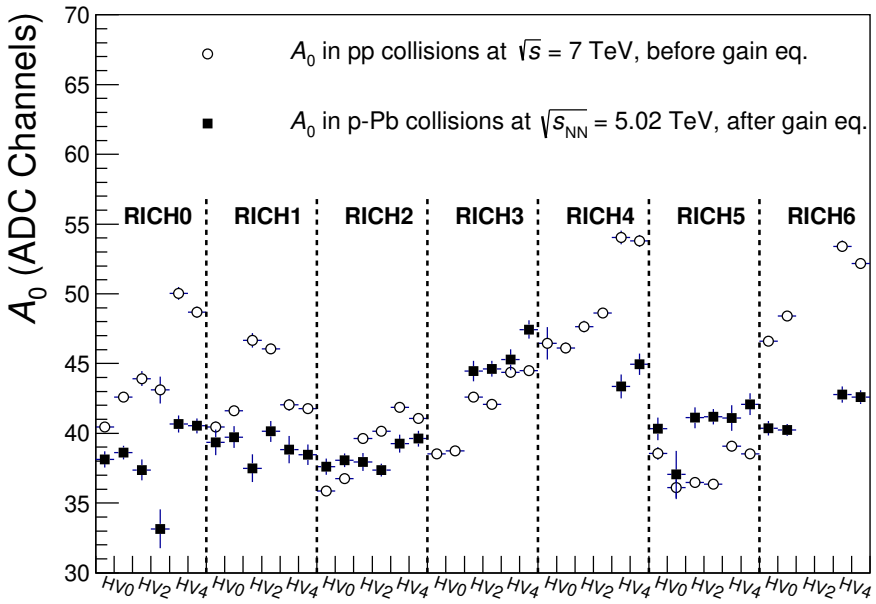

Fig. 12: A_0 values (proportional to the chamber gain) for the various HV sectors of each RICH module (for clearness only bins corresponding to even HV sectors are labelled) before the gain equalization (empty circles) and after the gain equalization (filled squares). HV sector 0 is at the bottom of the chamber, HV sector 5 is the upper one.

procedure (values in the range 2025-2055 V). The goal of this procedure was to reduce A_0 to ≈ 35 ADC channels (the design value is 30 ADC channels) and to reduce the gain spread down to 12%. As from 2012 the spread of points in the same data taking period remains constant, confirming the stability of the HV equalization. The observed average gain variations for each module as a function of time of about 15% are mainly related to change of atmospheric pressure since the temperature in the ALICE solenoid remained stable. After the HV equalization a better uniformity over the full detector is obtained, as can be observed in Fig. 12 (filled squares). On the average the higher A_0 values in the RICH3 is most probably due to mechanical tolerances of the MWPC aluminium frames. A smaller anode-cathode gap with the same HV setting, can increase the gas gain of the entire MWPC.

3.7 Stability of the CsI photocathodes

During the photocathode production (2001−2006), the CsI QE was measured via a Vacuum Ultraviolet (VUV) scanner [17, 18]. Only photocathodes satisfying some selection criteria (QE above a certain threshold and uniformity) were installed in the MWPCs. The CsI QE after 15 years from the production (out of which 5 taking data) is discussed in this section. Since direct access to the PC is not possible an indirect method for the evaluation of the CsI QE was developed. It is based for each photocathode on the measurement of the average number of detected Cherenkov photons per ring ($N_{\rm ph}$), for particles at $\beta \approx 1$. $N_{\rm ph}$ depends on:

- the gas gain;
- the C_6F_{14} transparency;
- the CsI QE that in turn, depends on:

  the specific charge dose on the photocathodes;

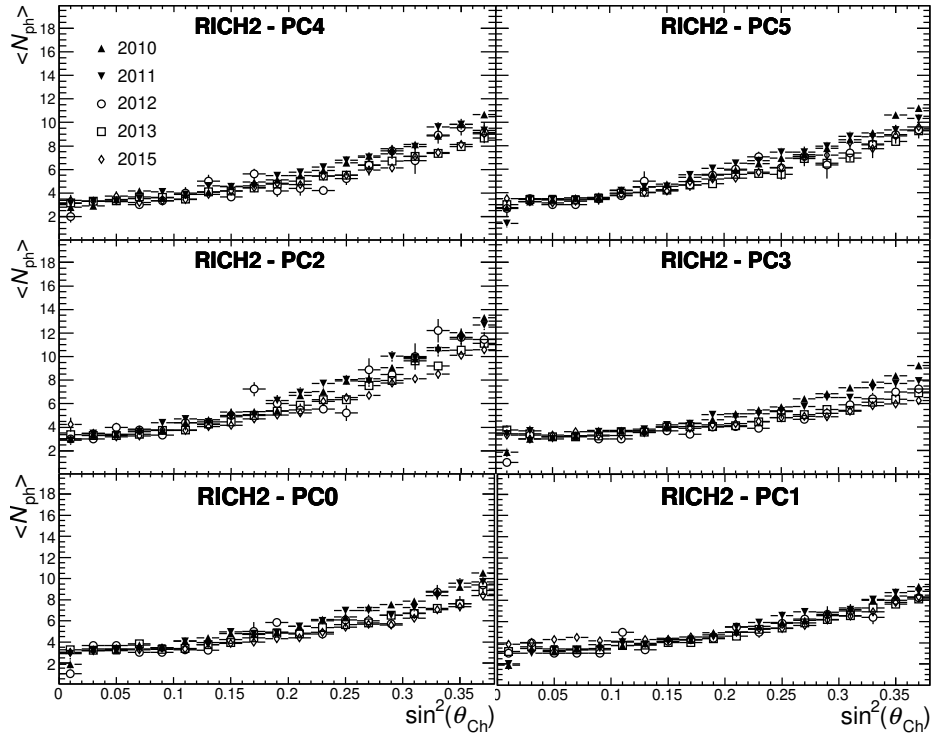

Fig. 13: Average number of detected Cherenkov photons per ring ($N_{\rm ph}$) as a function of the $\sin^2(\theta_{\rm Ch})$ for the six photocathodes of RICH 2, measured in the Run 1 and part of Run 2 data-taking periods.

O_2 and H_2O contaminants in the MWPC CH_4 gas;

the CsI physical-chemical aging process, if any.

The stability of $N_{\rm ph}$ ($\Delta N_{\rm ph} = 0$) after the equalization of the gas gain and the measured stability of the C_6F_{14} transparency enable to indirectly infer the stability of the QE. The charge dose below the limit for a possible loss of QE and the contaminants in the MWPC gas below the tolerated levels, would finally allow concluding that there is no physical-chemical aging of the CsI.

In Fig. 13 the $N_{\rm ph}$ as a function of $\sin^2\theta_{\rm Ch}$ for the six photocathodes of the RICH2, corrected by the single photoelectron (PE) detection efficiency (as calculated from eq. (1)) is shown. The correction by the detection efficiency is applied to take into account the gain variation. The values for the period 2012–2015 are a bit lower then the other since after the HV equalization gain decreased and the correction by the single photoelectron detection efficiency doesn't totally compensate the effect. The monitoring is performed by looking at the time evolution of the value of $N_{\rm ph}$ extracted in the interval $0.38 < \sin^2\theta_{\rm Ch} < 0.4$, where the Cherenkov angle is at the maximum value ($\cos(\theta_{\rm Ch}^{max}) \approx 1/n$). For this analysis only fully accepted Cherenkov photon rings are used. Although this selection provides adequate statistics for monitoring purposes, it doesn't allow us a direct comparison with the $N_{\rm ph}$ measured during the test beam at the production time of the photocathode (2001 to 2006). At that time only perpendicular tracks were selected. In Fig. 14, $N_{\rm ph}$ is shown per photocathode and per RICH module in the period 2010-2015.

The lower value of $N_{\rm ph}$ in RICH5 and RICH0 respectively on PC0-PC1 and PC2-PC3, is due to the not operational HV sectors. Incomplete rings are included in the analysis. Due to the excluded leaking radiator vessels and the failing HV sectors, only the PC4-5 of RICH4 are fully monitored.

The $N_{\rm ph}$ trends of Fig. 14 are fitted in the period 2011-2015 with linear functions (2010 data are excluded since taken before the HV equalization). The distribution of angular coefficients of the fit functions is reported in Fig. 15. The symmetric shape of this distribution and the mean value compatible with

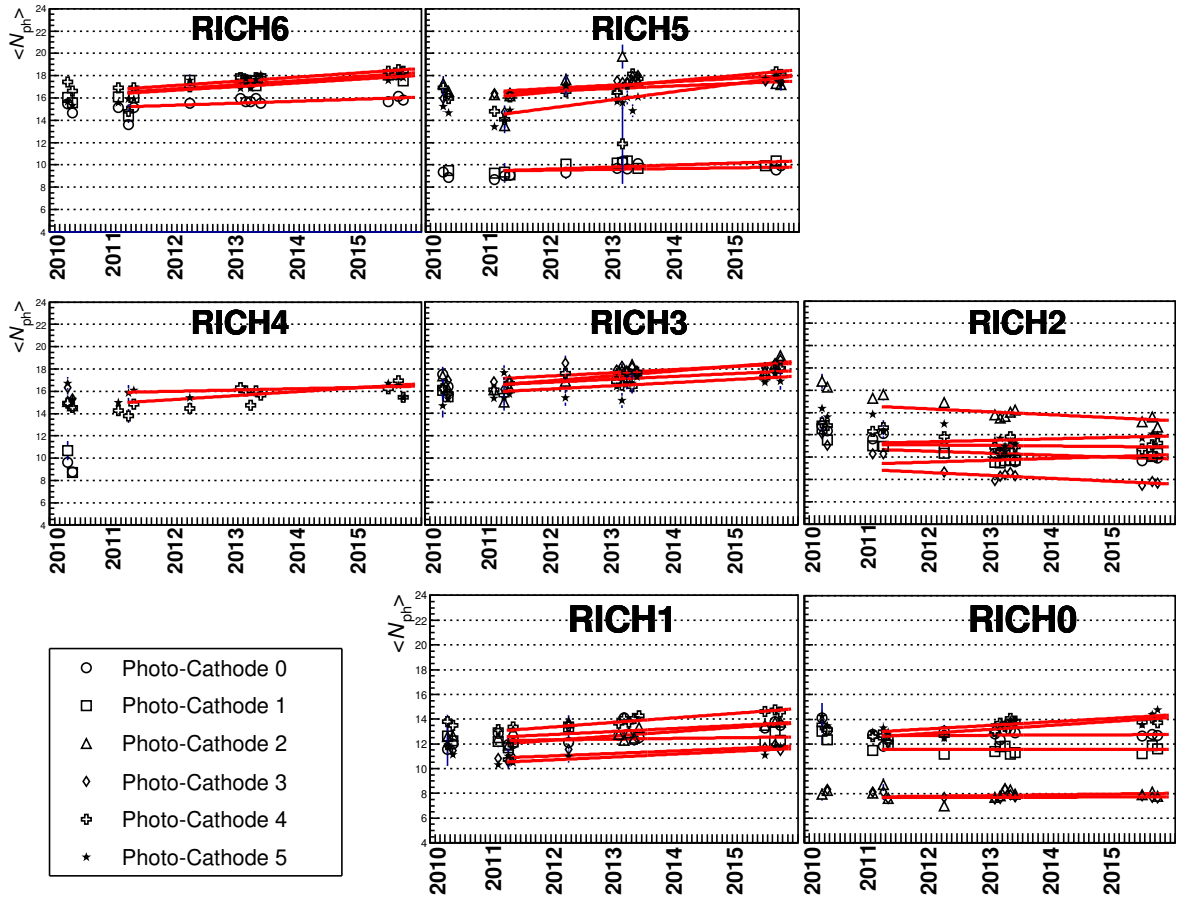

Fig. 14: Average number of reconstructed photons per track at the maximum Cherenkov angle per photocathode, as a function of the time, in pp and p–Pb collisions. A gas gain normalization factor was applied. To guide the eyes the fitting lines are shown.

zero demonstrate the stability of $N_{\rm ph}$. The slightly negative slope of PC0, PC2 and PC3 of RICH2 are of the same order of the positive slope in other modules and could be considered compatible with a stable photocathodes response (within the precision of this method). The observed stability of the C_6F_{14} transparency is an indication of the CsI QE stability over time. In addition, the presence of contaminants in the MWPC gas and the absorbed charge dose might have an effect on the CsI aging and this effect will be discussed in the next section.

3.7.1 Monitoring of the charge dose on the CsI

The RD26 and ALICE studies on the CsI aging due to the charge dose induced by avalanche ions demonstrated that this is an important parameter to monitor. Ultimately, it defines the lifetime of the detector. Several tests were carried out and the main results can be found in Refs. [9–11].

In order to calculate the charge dose in the period 2010−2015, the anode currents measured with the nano-ammeters of the HV channels are used. In Fig. 16, as an example, the distribution of the anode current $I_{\rm a}$ (in μA) for the RICH0-SECTOR0 and RICH0-SECTOR3 is shown. The $I_{\rm a}$ peaks at about 200 nA and 240 nA (black curve) correspond to the ramping up to the operational voltages. The peaks are produced when the HV cables and HV capacitors in the MWPC are charged up. The different peak position in BEAM TUNING and STABLE BEAM for the two channel is due to the different capacitive load (HV cable and HV decoupling capacitors) in the two channels. The red curve represents the $I_{\rm a}$ produced by the ionizing particles produced during the collisions and impinging on that sectors when

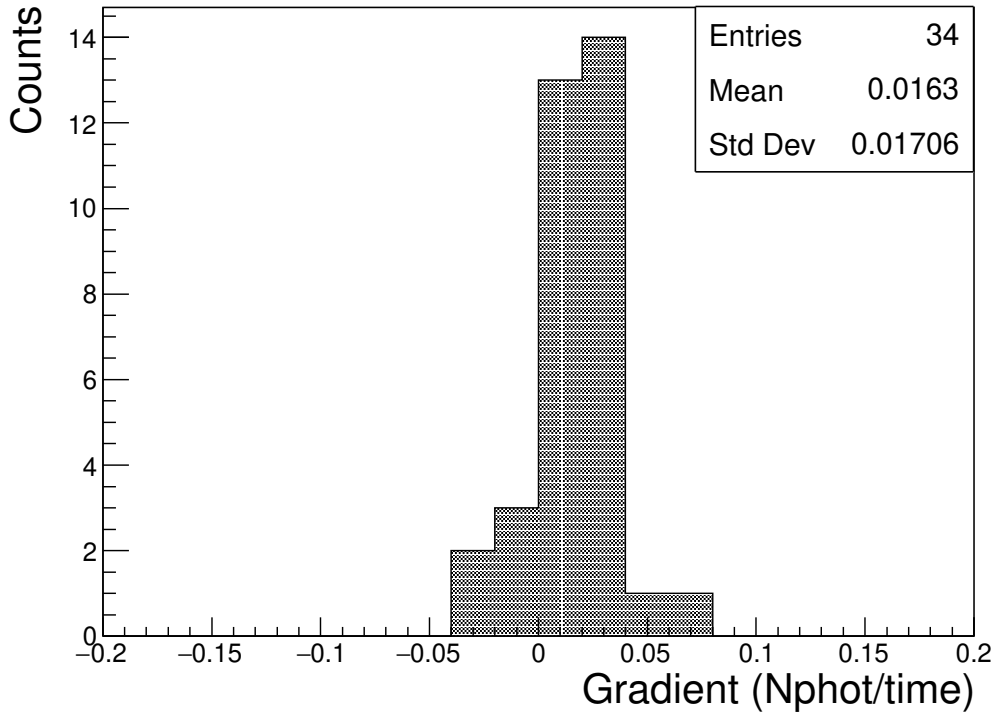

Fig. 15: Distribution of the slope parameters of the linear fit to the $\langle N_{\rm ph} \rangle$ trends shown in Fig. 14.

the HV is at its nominal value of about 2050 V. Some undesired samples around 200 nA survived since a more precise timing of the experiment-detector HV operation would be required. Nevertheless their contribution to the $I_{\rm a}$ is negligible since they are few entries in the logarithmic scale and in addition it goes in the conservative direction when the charge dose is calculated. In the HV sector 3, due to HV discharges, the voltage was set at 500 V (see Fig. 9) and the gas multiplication is not active, thus the red curve correspond only to the pedestal current. On the average they were at about 1nA on all over the 42 HV channels for the 7 RICH modules.

The specific charge dose on the CsI PCs is determined using 60% of the total anode current. This fraction is calculated by a simplified model that combines the contributions of ionizing particles and CsI photoelectrons. It assumes that half of the positive ion avalanches from the ionizing particles migrates towards the CsI photocathode whereas, conservatively, the full positive ion avalanches from CsI photoelectrons migrate towards the photocathode.

In Fig. 17 the sum of the charge doses of 2015 and 2010−2013 [19] is shown. A total average value of ≈ 0.02 mC/cm^2 per PC (full bars) is reached. This value is an order of magnitude below the limit of 0.2 mC/cm^2 for a possible CsI QE loss [10, 11]. As a consequence, an impact of the absorbed charge dose on the CsI QE can be excluded and the measured value is compatible with the observed stability of $N_{\rm ph}$. Figure 17 shows also the predictions for Run 3 and 4. In the Appendix A details on the model used for the charge dose calculation and its distribution over time in the period 2010−2015 can be found.

3.7.2 Monitoring of the CsI polluting agents

It is known that polluting agents as water and oxygen can affect the CsI QE. From extensive studies [7] it was concluded that exposure at the level of tens or hundreds of ppm does not degrade the CsI QE. Figure 18 shows the level of water and oxygen monitored through the DCS during the years 2010−2015. Their values of up to 2 ppm for water and 12 ppm for O_2 are well below the accepted limits and therefore

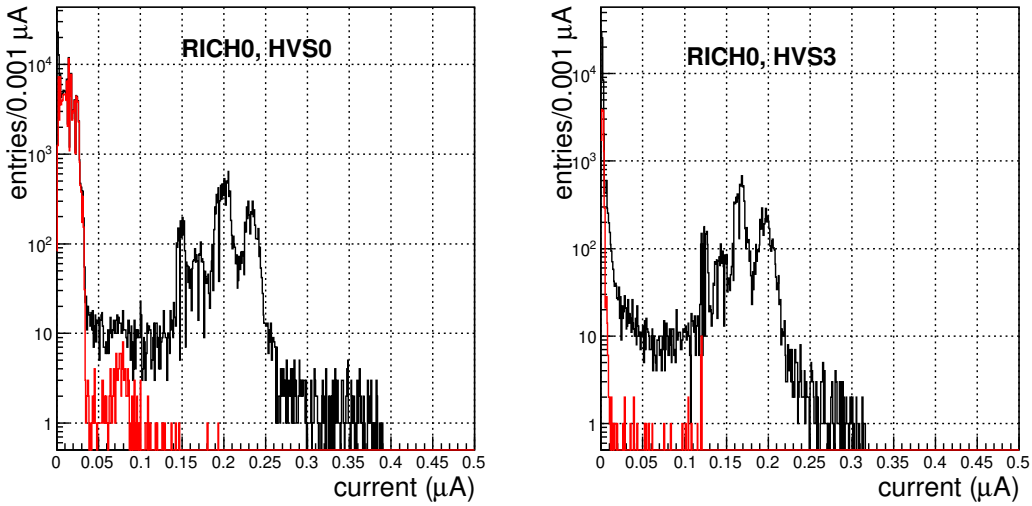

Fig. 16: In black: distribution of the anode current I_a (in μA) in two HV sector 3 of the RICH0 registered in the period 2011-2015. In red: I_a (in μA) excluding the HV ramp up phase and considering only the data with HV at the nominal value. The peak at about 70 nA in the left plot corresponds to high luminosity/background events. The plot on the right shows the current values of a failing HV sector, where gas multiplication is not active, so the red histogram is the current pedestal of the channel.

they do not have any impact on the CsI QE. The measured values are consistent with the observed stability of $\langle N_{ph} \rangle$.

3.7.3 CsI physical-chemical aging

The CsI physical-chemical aging would be measurable only exploiting photocathodes not exposed to any charge dose nor contaminants. At present, this direct measurement cannot be done. On the base of the observed stability and the analysis reported in the previous paragraphs it is possible to conclude that after 10 years from the production date for the majority of the photocathodes, no physical-chemical aging is affecting the CsI photocathodes.

4 Particle identification performance

The HMPID identifies charged hadrons by combining the emission angle of Cherenkov photons with the momentum measurement provided by the ALICE tracking devices. The HMPID PID in the momentum interval 1−5 GeV/c, effectively contributes in the measurement of the inclusive charged hadron production, and to the identification of light nuclei (deuteron in the momentum interval 3−8 GeV/c).

4.1 Pattern recognition algorithm

The measurement of the Cherenkov photon angles requires the track extrapolation from the central tracking devices (the Inner Tracking System (ITS) and the Time Projection Chamber (TPC)) up to the corresponding cluster on the HMPID photocathode. This cluster is called minimum ionizing particle (MIP) cluster in the rest of the document.

Starting from the centroid of the MIP cluster and scanning around candidate photon clusters, the Cherenkov emission angles are calculated. This procedure is called back-tracing [3]. To associate the average emission angle to the track and reject the background contribution, the Hough Transform Method (HTM) is applied [3, 8]. The result of the pattern recognition procedure is shown in Fig. 19, in which the Cherenkov angle, θ_{Ch}, is reported as a function of the track momentum for pp collisions at $\sqrt{s}$ = 13 TeV. The three

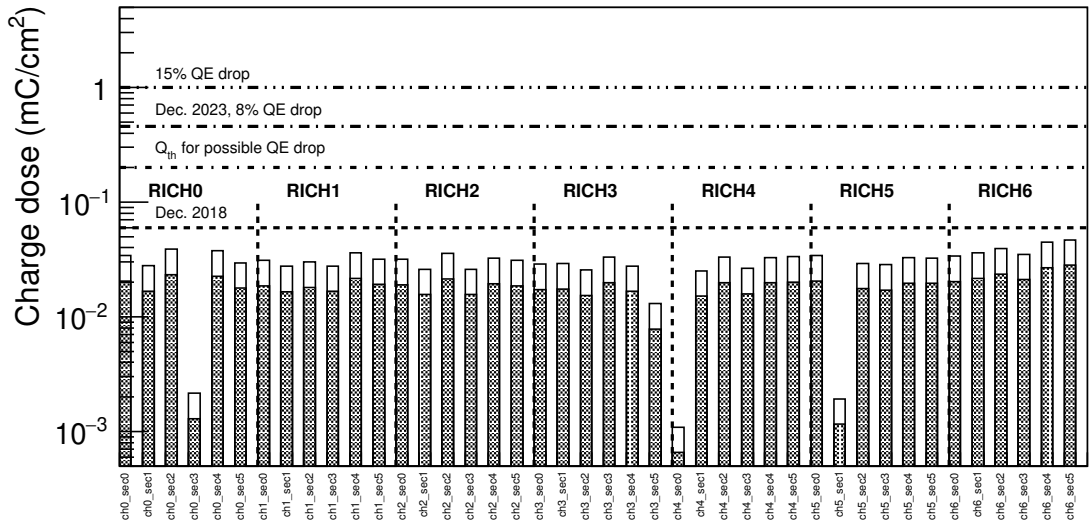

Fig. 17: Distribution of the specific charged dose on the 42 HV sectors of the HMPID absorbed during the LHC run period 2010-2015. The ch0-6 notation in the bin labels correspond to the modules RICH0-6. The full bars represent the CsI charge dose as calculated according to the model. The empty bars represent the total delivered specific charge dose (cathode wires and CsI photocathode). The HV sectors switched OFF, respectively RICH0-HVs3, RICH4-HVs0 and RICH5-HVs1, show the absorbed dose due to the HV channel pedestal values. The expected absorbed charge dose until the end of Run 2 (December 2018) and Run 3 (December 2023) data-taking periods, are also shown.

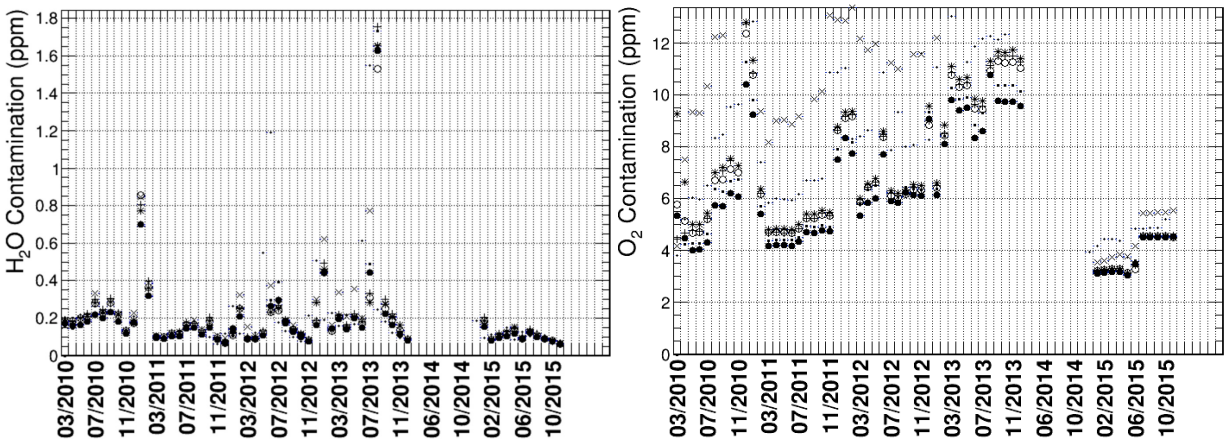

Fig. 18: Water (left) and oxygen (right) contaminations in the MWPC gas in the period 2010-2015. The different symbols correspond to the different HMPID modules.

visible bands correspond to pion, kaon and (anti-)proton signals. The experimental values are in good agreement with the theoretical curves. In pp and p–Pb collisions the track multiplicity in the HMPID acceptance corresponds to an average detector occupancy of $\approx 0.1\%$. Figure 20 shows the primary track multiplicity in Pb–Pb collisions at $\sqrt{s_{\rm NN}}$ = 5.02 TeV as a function of the collision centrality. The track multiplicityfaliroo produced in the most central (0-5%) Pb–Pb collisions, corresponds to an average detector occupancy of $\approx 3.5\%$. In these conditions the probability that the HTM algorithm detects fake Cherenkov patterns increases. Figure 21 shows the Cherenkov angles as a function of the track momentum in the most central ($0-10\%$) Pb–Pb collisions at $\sqrt{s_{\rm NN}}$ = 5.02 TeV. Although a non-negligible background contribution is present, the three bands of pions, kaons and (anti-)protons are clearly visible.

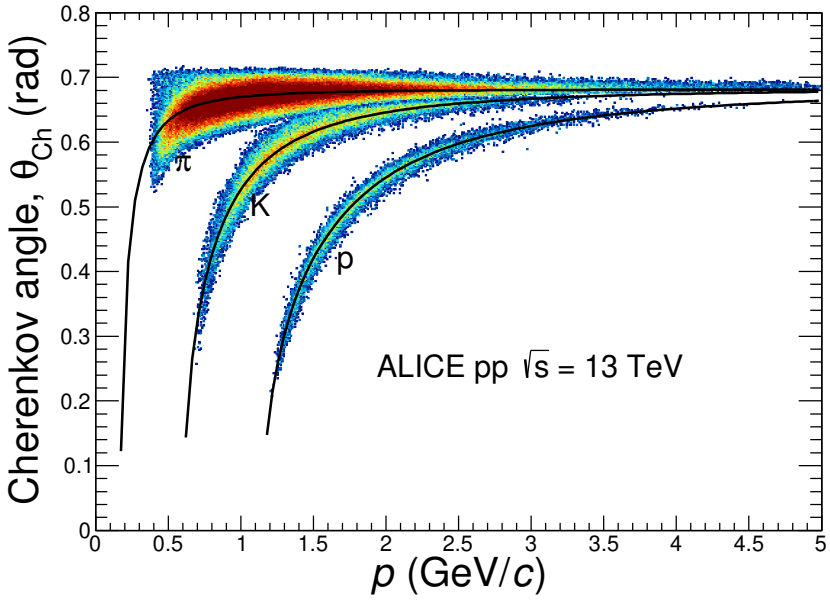

Fig. 19: Cherenkov angle reconstructed with the HMPID as a function of the track momentum for pp collisions at $\sqrt{s}$ = 13 TeV. The continuous lines represent the theoretical curves.

4.2 Particle identification approaches

Particle identification with HMPID can be performed using two different approaches: on a statistical basis and on a track-by-track basis. To extract the particle yields for identified hadron production studies, the statistical approach is used. The track-by-track approach can be used in the case of jet physics studies, which requires the identification of the jet leading particle, or in the case of identified hadron correlation studies.

4.2.1 Identification on statistical basis

In pp and p–Pb collisions, due to the low track multiplicity, the particle raw yields can be extracted by a triple-Gaussian fit to the Cherenkov angle distribution as shown in Fig. 22 for the transverse momentum intervals $2.5 < p_{\mathrm{T}} < 2.6$ GeV/c and $3.8 < p_{\mathrm{T}} < 4.0$ GeV/c.

The fit function used is the following:

$$f(\theta) = \frac{Y_{\pi}}{\sigma_{\pi}\sqrt{2\pi}} \mathrm{e}^{-\frac{(\theta-<\theta_{\pi}>)^2}{2\sigma_{\pi}^2}} + \frac{\mathrm{Y_K}}{\sigma_{\mathrm{K}}\sqrt{2\pi}} \mathrm{e}^{-\frac{(\theta-<\theta_{\mathrm{K}}>)^2}{2\sigma_{\mathrm{K}}^2}} + \frac{\mathrm{Y_p}}{\sigma_{\mathrm{p}}\sqrt{2\pi}} \mathrm{e}^{-\frac{(\theta-<\theta_{\mathrm{p}}>)^2}{2\sigma_{\mathrm{p}}^2}} \tag{2}$$

Where $\langle\theta_i\rangle$ and σ_i, (with i = π, K, p) are the means and the standard deviations of the Cherenkov angle distributions of the three hadron species, respectively. Y_i represents the integral of the three-Gaussian functions, i.e. the raw particle yields to be evaluated. The mean and standard deviation values for the three different particle hypothesis are deduced from the expected Cherenkov trend and MC simulation, and fixed in the fit function (eq. (2)) in order to extract the particle yields.

In the most central Pb–Pb collisions, due to the high number of primary and secondary tracks, the three Gaussian distributions for pions, kaons and (anti-)protons in a narrow transverse momentum interval, sit on a background distribution produced by identification of fake Cherenkov patterns in the high occupancy events (Fig. 23, yellow curve). A polynomial function of 6^{th} order is used to fit and subtract the background contribution from the θ_{Ch} distribution. The shoulder in the distributions starting at 0.7 rad is

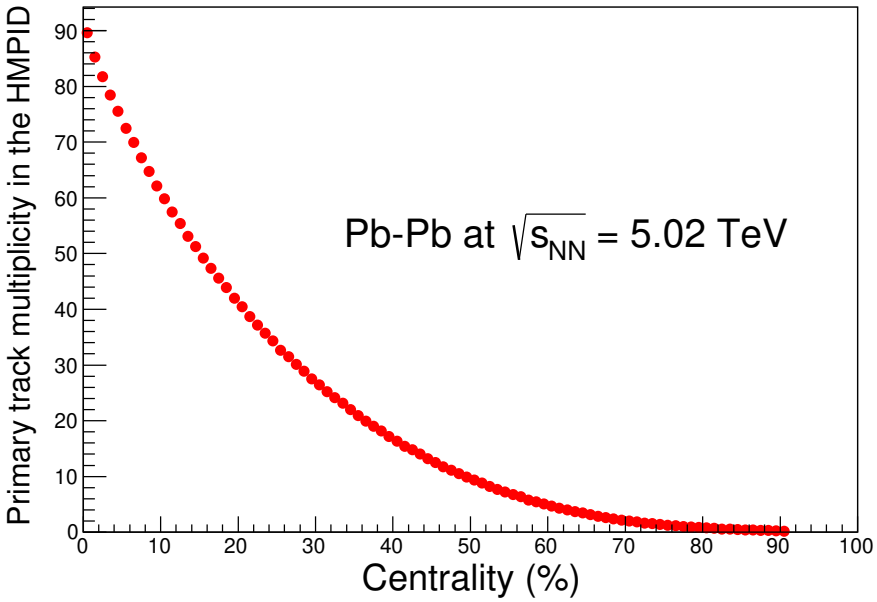

Fig. 20: Primary track multiplicity measured in the HMPID acceptance in Pb–Pb collisions at $\sqrt{s_{\rm NN}}$ = 5.02 TeV as a function of the collision centrality.

a boundary effect due to the finite geometrical acceptance of the chamber.

Figure 24 shows the separation in units of standard deviation (σ) for π/K and K/p in the HMPID as a function of the transverse momentum, for pp collisions at $\sqrt{s}$ = 13 TeV and in the 5% most central Pb–Pb collisions at $\sqrt{s_{\rm NN}}$ = 5.02 TeV. The precision of the fit of the background distribution represents a source of systematic uncertainty. For example, in the most central Pb–Pb collisions at $\sqrt{s_{\rm NN}}$ = 2.76 TeV. and at low transverse momenta (1.5 GeV/c), the systematic uncertainty due to the background subtraction amounts to $\approx$ 15% for pions and $\approx$ 8% for kaons and (anti-)protons [20]. In pp and p–Pb collisions where the background is negligible (Fig. 22) and the background fit is not needed, the total systematic uncertainty is smaller ($< \approx$ 12%).

Exploiting the statistical unfolding, the HMPID provided pion and kaon $p_{\rm T}$ spectra between 1.5 GeV/c and 4 GeV/c and (anti-)proton spectra in the $p_{\rm T}$ interval 1.5$-$6 GeV/c. The analysis was performed for pp, p–Pb and Pb–Pb collision data [20–23] collected during the LHC Run 1 data-taking period. In the most central Pb–Pb collisions the HMPID reduces the uncertainties of the measurements in the region of transition between the identification by the Time-Of-Flight and the specific energy loss, dE/dx, in the relativistic rise region at $\approx$ 3 GeV/c. It thus improves the precision of the measurement and validates the other methods in the region where these techniques have worse PID performance.

4.2.2 Identification on a track-by-track basis

For the identification on a track-by-track basis, two PID estimators can be used:

- the probability that the particle is one of the known charged hadron species;
- the difference between the value of the measured Cherenkov angle and the theoretical one for known hadrons in units of the detector resolution (sigma).

The second estimator is defined as:

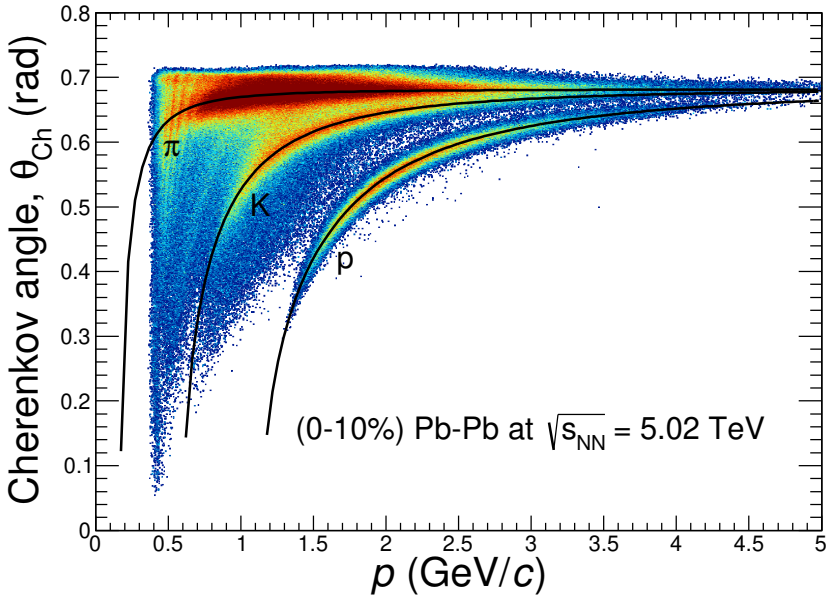

Fig. 21: Cherenkov angle reconstructed with the HMPID as a function of the track momentum for central (0-10%) Pb−Pb collisions at $\sqrt{s_{\rm NN}}$ = 5.02 TeV data. The continuous lines represent the theoretical curves.

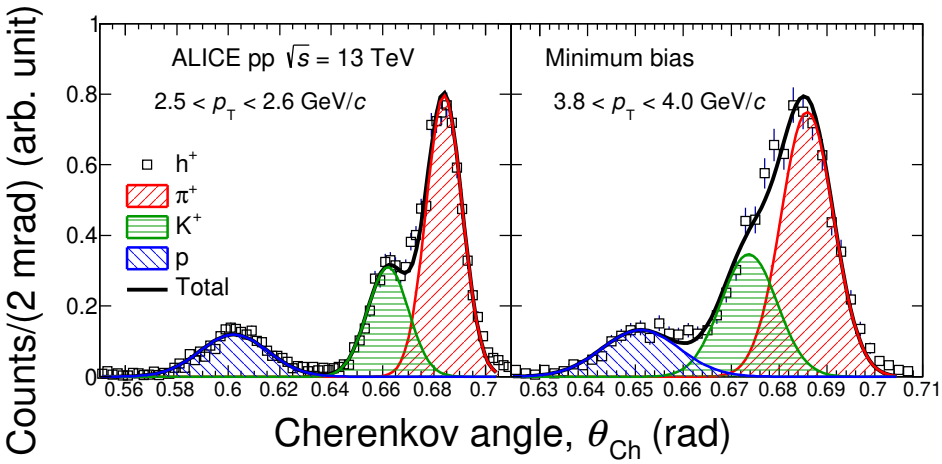

Fig. 22: Distributions of the Cherenkov angle measured in the HMPID for positive tracks with $p_{\rm T}$ in two intervals, 2.5-2.6 GeV/c (left) and 3.8-4.0 GeV/c (right), for pp collisions at $\sqrt{s}$ = 13 TeV data. The histograms are scaled to have a similar maximum value.

$$N_\sigma^i = \frac{|\theta_{\rm Ch}^{\rm exp} - \theta_{\rm Ch}^{i,{\rm theor}}|}{\sigma_i} \tag{3}$$

where $\theta_{\rm Ch}^{\rm exp}$ is the measured Cherenkov angle, $\theta_{\rm Ch}^{\rm i,theor}$ is the theoretical angle calculated for each mass hypothesis, and σ_i is the expected resolution extracted. from data. Selecting on N_σ^i variables it is possible to select a sample of identified hadrons with a given purity and contamination level, defined as:

$$p_{\rm i} = \frac{N_{\rm id}^{\rm t}(i)}{N_{\rm id}(i)}, \qquad c_{\rm i} = \frac{N_{\rm id}^{\rm w}(i)}{N_{\rm id}(i)} \tag{4}$$

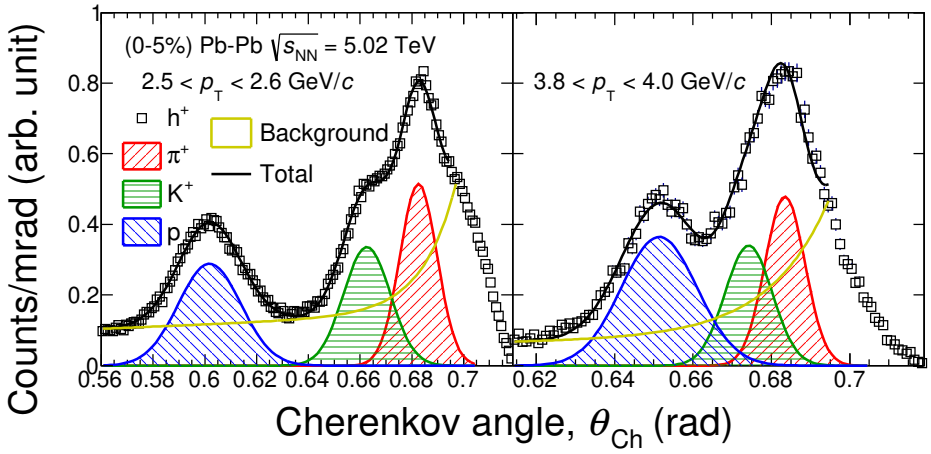

Fig. 23: Distributions of the Cherenkov angle measured in the HMPID for positive tracks with p_T in two intervals, 2.5-2.6 GeV/c (left) and 3.8-4.0 GeV/c (right), for Pb–Pb collisions at $\sqrt{s_{NN}}$ = 5.02 TeV, in the centrality class 0-5%. The histograms are scaled to have a similar maximum value.

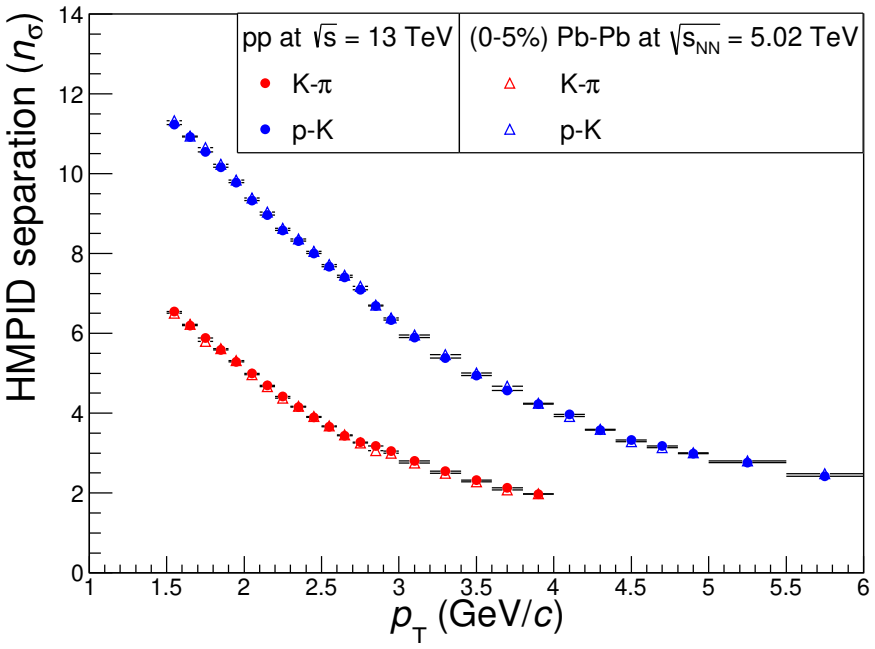

Fig. 24: The separation power in units of σ for π/K and K/p in the HMPID as a function of the transverse momentum, for pp collisions at $\sqrt{s}$ = 13 TeV and in 5% most central Pb–Pb collisions at $\sqrt{s_{NN}}$ = 5.02 TeV.

where $N_{id}(i)$ is the number of particles identified as of type i, $N^{t}_{id}(i)$ is the number of particles correctly identified while $N^{w}_{id}(i)$ is the number of particles mis-identified, with $i = \pi$, K, p.

In Fig. 25 the purity and the contamination of a sample of protons in Pb–Pb collisions in two different centrality intervals, obtained from a HIJING Monte Carlo simulation [24], identified by the HMPID requiring $|N^{p}_{\sigma}| < 2$ in Pb−Pb collisions, are shown. The simulation has been performed in the official framework of ALICE, AliRoot [25] and it reproduces very well the detector response. In the most central Pb–Pb collisions, the mis-identification probability is higher than in the more peripheral ones due to the higher charged track multiplicity. As a consequence the purity of the proton sample is lower in central Pb–Pb collisions than in peripheral ones.

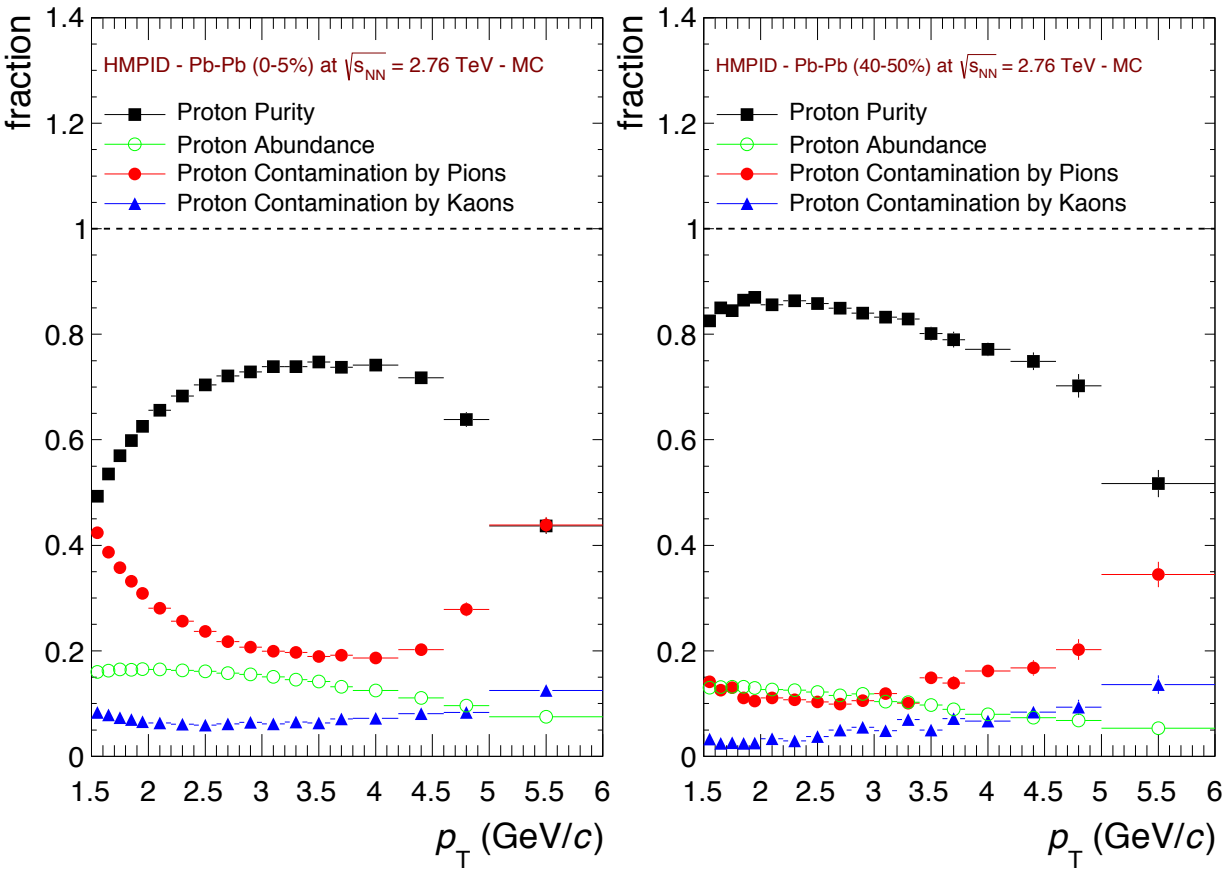

Fig. 25: Purity and contamination for identified protons obtained from a HIJING Monte Carlo simulation in Pb–Pb collisions at $\sqrt{s_{\rm NN}}$ = 2.76 TeV, in two different centrality intervals, 0-5% (left) and 40-50% (right).

4.3 Deuteron identification

Figure 26 shows the squared particle mass distribution calculated using the measured HMPID Cherenkov angle, in the most central (0-10%) Pb–Pb collisions at $\sqrt{s_{\rm NN}}$ = 5.02 TeV. The signal to background ratio for deuterons is large enough to allow its identification. The squared mass is calculated using the equation:

$$m^2 = p^2\left(n^2\cos^2\theta_{\rm Ch} - 1\right) \tag{5}$$

where p is the particle momentum measured by the ALICE tracking detectors and n is the radiator refractive index. In the squared mass distribution four peaks, corresponding to pions, kaons, (anti-)protons and deuterons, are clearly visible. The deuteron yield in the HMPID was measured in the transverse momentum interval 3−8 GeV/c. The yields have been combined with those measured by identifying the deuterons with the TPC and TOF in the common transverse momentum interval [26].

5 Perspective for the detector operation during 2022−2024

After ten years from the first operation, it can be concluded that the HMPID performance is stable and the PID capabilities are according to expectations

At the end of the LHC Run 3 data-taking period (2022−2024 HL-LHC, Run 3) with Pb–Pb runs at 50 kHz of collision rate an integrated specific charge dose on the CsI photocathodes of ≈ 0.2 mC/cm^2 is expected (see Fig. 17) and in these conditions, no CsI QE loss is expected [10]. If nevertheless needed,

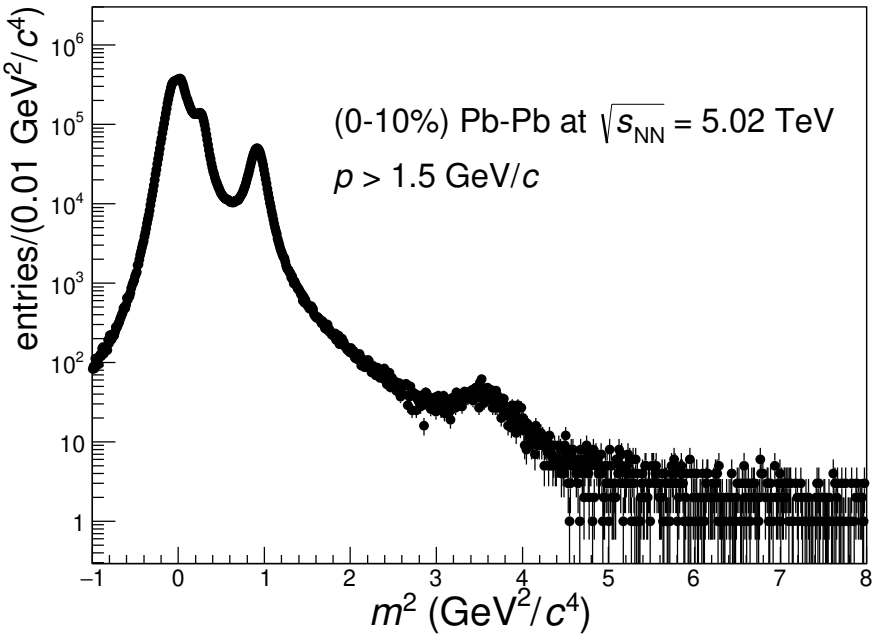

Fig. 26: Squared particle mass distribution obtained from the Cherenkov angle measured in the HMPID combined with the momentum information provided by the ALICE tracking devices, in central (0-10%) Pb–Pb collisions at $\sqrt{s_{NN}}$ = 5.02 TeV.

CsI QE loss at the level of few per cents can be compensated by increasing the photoelectrons detection efficiency obtained increasing the MWPC voltage.

Test results with an upgraded readout firmware have already shown that in pp collisions an event readout rate of 10 kHz can be achieved, doubling the current HMPID readout rate. In addition, the integration of the detector in the new ALICE systems [15, 27] is progressing well.

Therefore the HMPID will also contribute to the ALICE physics program in the LHC Run 3 data taking period.

For the participation of the HMPID detector to the LHC Run 4 data taking period (starting in 2026) a final decision will be taken at the end of 2024 on the basis of the general HMPID detector status.

6 Conclusions

The HMPID project has successfully proven that RICH detectors based on pad segmented CsI photocathodes in MWPC, can be operated over a time scale compatible with the runtime of experiments at colliders. With 10.3 m^2 of CsI active area, the HMPID, the largest detector based on this technology, has successfully participated in the ALICE physics program during the LHC run period 2010−2015. In this period the detector has shown good stability, in particular for the N_{ph}, the number of detected photon per track at the maximum Cherenkov angle. This is the evidence of the CsI QE stability and so far the demonstration of the absence of aging effects. The measured specific charge dose of 0.02 mC/cm^2 on the CsI photocathodes, the low level of O_2 and H_2O contaminants in the MWPC gas and the absence of CsI physical-chemical aging effects, are consistent with the observed stability of the CsI QE.

The charge dose so far accumulated and the additional one expected from the remaining LHC Run 2 data taking period and LHC Run 3 one, will result in a CsI charge absorbed dose of about 0.2 mC/cm^2, where no relevant CsI aging effects are expected.

The HMPID PID capability allowed pions, kaons, and (anti-)protons to be identified in the transverse momentum interval $1-5$ GeV/c in pp, p–Pb and Pb–Pb collisions. It contributed to the measurements of the identified charged hadron production (nuclear modification factor R_{AA}, spectra of identified particles), and on the deuteron identification [20–23, 26].

Given the good and stable detector performance the HMPID will participate to the Run 3 data taking period (2022-2024) with Pb–Pb runs at 50 kHz of collision rate.

The final decision for the HMPID participation in the Run 4 data-taking period will be taken at the end of 2024, on the basis of the general detector status.

Acknowledgements

The ALICE Collaboration would like to thank all its engineers and technicians for their invaluable contributions to the construction of the experiment and the CERN accelerator teams for the outstanding performance of the LHC complex. The ALICE Collaboration gratefully acknowledges the resources and support provided by all Grid centres and the Worldwide LHC Computing Grid (WLCG) collaboration. The ALICE Collaboration acknowledges the following funding agencies for their support in building and running the ALICE detector: A. I. Alikhanyan National Science Laboratory (Yerevan Physics Institute) Foundation (ANSL), State Committee of Science and World Federation of Scientists (WFS), Armenia; Austrian Academy of Sciences, Austrian Science Fund (FWF): [M 2467-N36] and Nationalstiftung für Forschung, Technologie und Entwicklung, Austria; Ministry of Communications and High Technologies, National Nuclear Research Center, Azerbaijan; Conselho Nacional de Desenvolvimento Científico e Tecnológico (CNPq), Financiadora de Estudos e Projetos (Finep), Fundação de Amparo à Pesquisa do Estado de São Paulo (FAPESP) and Universidade Federal do Rio Grande do Sul (UFRGS), Brazil; Ministry of Education of China (MOEC) , Ministry of Science & Technology of China (MSTC) and National Natural Science Foundation of China (NSFC), China; Ministry of Science and Education and Croatian Science Foundation, Croatia; Centro de Aplicaciones Tecnológicas y Desarrollo Nuclear (CEADEN), Cubaenergía, Cuba; Ministry of Education, Youth and Sports of the Czech Republic, Czech Republic; The Danish Council for Independent Research | Natural Sciences, the VILLUM FONDEN and Danish National Research Foundation (DNRF), Denmark; Helsinki Institute of Physics (HIP), Finland; Commissariat à l'Energie Atomique (CEA) and Institut National de Physique Nucléaire et de Physique des Particules (IN2P3) and Centre National de la Recherche Scientifique (CNRS), France; Bundesministerium für Bildung und Forschung (BMBF) and GSI Helmholtzzentrum für Schwerionenforschung GmbH, Germany; General Secretariat for Research and Technology, Ministry of Education, Research and Religions, Greece; National Research, Development and Innovation Office, Hungary; Department of Atomic Energy Government of India (DAE), Department of Science and Technology, Government of India (DST), University Grants Commission, Government of India (UGC) and Council of Scientific and Industrial Research (CSIR), India; Indonesian Institute of Science, Indonesia; Istituto Nazionale di Fisica Nucleare (INFN), Italy; Japanese Ministry of Education, Culture, Sports, Science and Technology (MEXT), Japan Society for the Promotion of Science (JSPS) KAKENHI and Japanese Ministry of Education, Culture, Sports, Science and Technology (MEXT)of Applied Science (IIST), Japan; Consejo Nacional de Ciencia (CONACYT) y Tecnología, through Fondo de Cooperación Internacional en Ciencia y Tecnología (FONCICYT) and Dirección General de Asuntos del Personal Academico (DGAPA), Mexico; Nederlandse Organisatie voor Wetenschappelijk Onderzoek (NWO), Netherlands; The Research Council of Norway, Norway; Commission on Science and Technology for Sustainable Development in the South (COMSATS), Pakistan; Pontificia Universidad Católica del Perú, Peru; Ministry of Education and Science, National Science Centre and WUT ID-UB, Poland; Korea Institute of Science and Technology Information and National Research Foundation of Korea (NRF), Republic of Korea; Ministry of Education and Scientific Research, Institute of Atomic Physics and Ministry of Research

and Innovation and Institute of Atomic Physics, Romania; Joint Institute for Nuclear Research (JINR), Ministry of Education and Science of the Russian Federation, National Research Centre Kurchatov Institute, Russian Science Foundation and Russian Foundation for Basic Research, Russia; Ministry of Education, Science, Research and Sport of the Slovak Republic, Slovakia; National Research Foundation of South Africa, South Africa; Swedish Research Council (VR) and Knut & Alice Wallenberg Foundation (KAW), Sweden; European Organization for Nuclear Research, Switzerland; Suranaree University of Technology (SUT), National Science and Technology Development Agency (NSDTA) and Office of the Higher Education Commission under NRU project of Thailand, Thailand; Turkish Energy, Nuclear and Mineral Research Agency (TENMAK), Turkey; National Academy of Sciences of Ukraine, Ukraine; Science and Technology Facilities Council (STFC), United Kingdom; National Science Foundation of the United States of America (NSF) and United States Department of Energy, Office of Nuclear Physics (DOE NP), United States of America.

References

[1] **ALICE** Collaboration, K. Aamodt *et al.*, "The ALICE experiment at the CERN LHC", *JINST* **3** (2008) S08002.

[2] **ALICE** Collaboration, B. B. Abelev *et al.*, "Performance of the ALICE Experiment at the CERN LHC", *Int. J. Mod. Phys. A* **29** (2014) 1430044, arXiv:1402.4476 [nucl-ex].

[3] **ALICE** Collaboration, S. Beole *et al.*, "ALICE technical design report: Detector for high momentum PID",. http://cds.cern.ch/record/381431?ln=it.

[4] **COMPASS** Collaboration, G. Baum *et al.*, "COMPASS: A Proposal for a Common Muon and Proton Apparatus for Structure and Spectroscopy",. http://cds.cern.ch/record/298433/files/B00005486.pdf.

[5] P. Salabura *et al.*, "Hades experiments: investigation of hadron in-medium properties", *Journal of Physics: Conference Series* **420** (Mar, 2013) 012013. https://doi.org/10.1088/1742-6596/420/1/012013.

[6] Y. Andres *et al.*, "R & D in ALICE: The CsI-based RICH high momentum particle identification detector", *Eur. Phys. J.direct* **4** no. S1, (2002) 25.

[7] F. Piuz, "Ring Imaging CHerenkov systems based on gaseous photo-detectors: Trends and limits around particle accelerators", *Nucl. Instrum. Meth.* **A502** (2003) 76–90.

[8] **ALICE** Collaboration, D. Di Bari, "The pattern recognition method for the CsI-RICH detector in ALICE", *Nucl. Instrum. Meth.* **A502** (2003) 300–304.

[9] H. Hoedlmoser *et al.*, "Quality evaluation of CsI photocathodes for the ALICE / HMPID detector", *Nucl. Instrum. Meth.* **A553** (2005) 140–145.

[10] A. Braem *et al.*, "Results from the ageing studies of large CsI photocathodes exposed to ionizing radiation in a gaseous RICH detector", *Nucl. Instrum. Meth.* **A553** (2005) 187–195.

[11] H. Hoedlmoser *et al.*, "Long term performance and ageing of CsI photocathodes for the ALICE/HMPID detector", *Nucl. Instrum. Meth.* **A574** (2007) 28–38.

[12] G. De Cataldo, A. Franco, C. Pastore, I. Sgura, and G. Volpe, "The ALICE-HMPID detector control system: Its evolution towards an expert and adaptive system", *Nucl. Instrum. Meth.* **A639** (2011) 211–214.

[13] **ALICE** Collaboration, J.-C. Santiard and K. Marent, "The Gassiplex0.7-2 Integrated Front-End Analog Processor for the HMPID and the Dimuon Spectrometer of ALICE",. http://cds.cern.ch/record/523473.

[14] J. C. Santiard, "The ALICE HMPID on-detector front-end and readout electronics", *Nucl. Instrum. Meth.* **A518** (2004) 498–500.

[15] **ALICE** Collaboration, P. Antonioli, A. Kluge, and W. Riegler, "Upgrade of the ALICE Readout & Trigger System",. http://cds.cern.ch/record/1603472/files/ALICE-TDR-015.pdf.

[16] E. Albrecht *et al.*, "Perfluorocarbon effects on composite and polymeric materials used within RICH detectors",. http://cds.cern.ch/record/2628814.

[17] H. Hoedlmoser *et al.*, "Production technique and quality evaluation of CsI photocathodes for the ALICE/HMPID detector", *Nucl. Instrum. Meth.* **A566** (2006) 338–350.

[18] H. Hoedlmoser *et al.*, "Photo-current scanner system for in situ quality assessment of large area CsI photocathodes", *Nucl. Instrum. Meth.* **A566** (2006) 351–359.

[19] **ALICE** Collaboration, G. De Cataldo, "The ALICE–HMPID performance during the LHC run period 2010–2013", *Nucl. Instrum. Meth.* **A766** (2014) 19–21.

[20] **ALICE** Collaboration, J. Adam *et al.*, "Centrality dependence of the nuclear modification factor of charged pions, kaons, and protons in Pb-Pb collisions at $\sqrt{s_{\rm NN}} = 2.76$ TeV", *Phys. Rev.* **C93** no. 3, (2016) 034913, arXiv:1506.07287 [nucl-ex].

[21] **ALICE** Collaboration, J. Adam *et al.*, "Measurement of pion, kaon and proton production in proton–proton collisions at $\sqrt{s} = 7$ TeV", *Eur. Phys. J.* **C75** no. 5, (2015) 226, arXiv:1504.00024 [nucl-ex].

[22] **ALICE** Collaboration, B. B. Abelev *et al.*, "Production of charged pions, kaons and protons at large transverse momenta in pp and Pb–Pb collisions at $\sqrt{s_{\rm NN}}$ =2.76 TeV", *Phys. Lett.* **B736** (2014) 196–207, arXiv:1401.1250 [nucl-ex].

[23] **ALICE** Collaboration, J. Adam *et al.*, "Multiplicity dependence of charged pion, kaon, and (anti)proton production at large transverse momentum in p-Pb collisions at $\sqrt{s_{\rm NN}}$ = 5.02 TeV", *Phys. Lett.* **B760** (2016) 720–735, arXiv:1601.03658 [nucl-ex].

[24] M. Gyulassy and X.-N. Wang, "HIJING 1.0: A Monte Carlo program for parton and particle production in high-energy hadronic and nuclear collisions", *Comput. Phys. Commun.* **83** (1994) 307, arXiv:nucl-th/9502021 [nucl-th].

[25] http://AliSoft.cern.ch/offline/.

[26] **ALICE** Collaboration, S. Acharya *et al.*, "Measurement of deuteron spectra and elliptic flow in Pb–Pb collisions at $\sqrt{s_{\rm NN}}$ = 2.76 TeV at the LHC", *Eur. Phys. J. C* **77** no. 10, (2017) 658, arXiv:1707.07304 [nucl-ex].

[27] **ALICE** Collaboration, P. Buncic, M. Krzewicki, and P. Vande Vyvre, "Technical Design Report for the Upgrade of the Online-Offline Computing System",. http://cds.cern.ch/record/2011297/files/ALICE-TDR-019.pdf.

A The ALICE Collaboration

ALICE Collaboration

S. Acharya[142], D. Adamová[97], A. Adler[75], J. Adolfsson[82], G. Aglieri Rinella[34], M. Agnello[30], N. Agrawal[54], Z. Ahammed[142], S. Ahmad[16], S.U. Ahn[77], I. Ahuja[38], Z. Akbar[51], A. Akindinov[94], M. Al-Turany[109], S.N. Alam[16], D. Aleksandrov[90], B. Alessandro[60], H.M. Alfanda[7], R. Alfaro Molina[72], B. Ali[16], Y. Ali[14], A. Alici[25], N. Alizadehvandchali[126], A. Alkin[34], J. Alme[21], G. Alocco[55], T. Alt[69], I. Altsybeev[114], M.N. Anaam[7], C. Andrei[48], D. Andreou[92], A. Andronic[145], M. Angeletti[34], V. Anguelov[106], F. Antinori[57], P. Antonioli[54], C. Anuj[16], N. Apadula[81], L. Aphecetche[116], H. Appelshäuser[69], S. Arcelli[25], R. Arnaldi[60], I.C. Arsene[20], M. Arslandok[147], A. Augustinus[34], R. Averbeck[109], S. Aziz[79], M.D. Azmi[16], A. Badalà[56], Y.W. Baek[41], X. Bai[130,109], R. Bailhache[69], Y. Bailung[50], R. Bala[103], A. Balbino[30], A. Baldisseri[139], B. Balis[2], D. Banerjee[4], R. Barbera[26], L. Barioglio[107], M. Barlou[86], G.G. Barnaföldi[146], L.S. Barnby[96], V. Barret[136], C. Bartels[129], K. Barth[34], E. Bartsch[69], F. Baruffaldi[27], N. Bastid[136], S. Basu[82], G. Batigne[116], B. Batyunya[76], D. Bauri[49], J.L. Bazo Alba[113], I.G. Bearden[91], C. Beattie[147], P. Becht[109], I. Belikov[138], A.D.C. Bell Hechavarria[145], F. Bellini[25], R. Bellwied[126], S. Belokurova[114], V. Belyaev[95], G. Bencedi[146,70], S. Beole[24], A. Bercuci[48], Y. Berdnikov[100], A. Berdnikova[106], L. Bergmann[106], M.G. Besoiu[68], L. Betev[34], P.P. Bhaduri[142], A. Bhasin[103], I.R. Bhat[103], M.A. Bhat[4], B. Bhattacharjee[42], P. Bhattacharya[22], L. Bianchi[24], N. Bianchi[52], J. Bielčík[37], J. Bielčíková[97], J. Biernat[119], A. Bilandzic[107], G. Biro[146], S. Biswas[4], J.T. Blair[120], D. Blau[90,83], M.B. Blidaru[109], C. Blume[69], G. Boca[28,58], F. Bock[98], A. Bogdanov[95], S. Boi[22], J. Bok[62], L. Boldizsár[146], A. Bolozdynya[95], M. Bombara[38], P.M. Bond[34], G. Bonomi[141,58], H. Borel[139], A. Borissov[83], H. Bossi[147], E. Botta[24], L. Bratrud[69], P. Braun-Munzinger[109], M. Bregant[122], M. Broz[37], G.E. Bruno[108,33], M.D. Buckland[129], D. Budnikov[110], H. Buesching[69], S. Bufalino[30], O. Bugnon[116], P. Buhler[115], Z. Buthelezi[73,133], J.B. Butt[14], A. Bylinkin[128], S.A. Bysiak[119], M. Cai[27,7], H. Caines[147], A. Caliva[109], E. Calvo Villar[113], J.M.M. Camacho[121], R.S. Camacho[45], P. Camerini[23], F.D.M. Canedo[122], F. Carnesecchi[34,25], R. Caron[139], J. Castillo Castellanos[139], E.A.R. Casula[22], F. Catalano[30], C. Ceballos Sanchez[76], P. Chakraborty[49], S. Chandra[142], S. Chapeland[34], M. Chartier[129], S. Chattopadhyay[142], S. Chattopadhyay[111], A. Chauvin[22], T.G. Chavez[45], T. Cheng[7], C. Cheshkov[137], B. Cheynis[137], V. Chibante Barroso[34], D.D. Chinellato[123], S. Cho[62], P. Chochula[34], P. Christakoglou[92], C.H. Christensen[91], P. Christiansen[82], T. Chujo[135], C. Cicalo[55], L. Cifarelli[25], F. Cindolo[54], M.R. Ciupek[109], G. Clai[II,54], J. Cleymans[I,125], F. Colamaria[53], J.S. Colburn[112], D. Colella[53,108,33], A. Collu[81], M. Colocci[34], M. Concas[III,60], G. Conesa Balbastre[80], Z. Conesa del Valle[79], G. Contin[23], J.G. Contreras[37], M.L. Coquet[139], T.M. Cormier[98], P. Cortese[31], M.R. Cosentino[124], F. Costa[34], S. Costanza[28,58], P. Crochet[136], R. Cruz-Torres[81], E. Cuautle[70], P. Cui[7], L. Cunqueiro[98], A. Dainese[57], M.C. Danisch[106], A. Danu[68], P. Das[88], P. Das[4], S. Das[4], S. Dash[49], A. De Caro[29], G. de Cataldo[53], L. De Cilladi[24], J. de Cuveland[39], A. De Falco[22], D. De Gruttola[29], N. De Marco[60], C. De Martin[23], S. De Pasquale[29], S. Deb[50], H.F. Degenhardt[122], K.R. Deja[143], C. Dell'Olio[33], D. Dell'Olio[33], L. Dello Stritto[29], W. Deng[7], P. Dhankher[19], D. Di Bari[33], A. Di Mauro[34], R.A. Diaz[8], T. Dietel[125], Y. Ding[137,7], R. Divià[34], D.U. Dixit[19], Ø. Djuvsland[21], U. Dmitrieva[64], J. Do[62], A. Dobrin[68], B. Dönigus[69], A.K. Dubey[142], A. Dubla[109,92], S. Dudi[102], M. Dukhishyam[88], P. Dupieux[136], N. Dzalaiova[13], T.M. Eder[145], R.J. Ehlers[98], V.N. Eikeland[21], F. Eisenhut[69], D. Elia[53], B. Erazmus[116], F. Ercolessi[25], F. Erhardt[101], A. Erokhin[114], M.R. Ersdal[21], B. Espagnon[79], G. Eulisse[34], D. Evans[112], S. Evdokimov[93], L. Fabbietti[107], M. Faggin[27], J. Faivre[80], F. Fan[7], A. Fantoni[52], M. Fasel[98], P. Fecchio[30], A. Feliciello[60], G. Feofilov[114], A. Fernández Téllez[45], A. Ferrero[139], A. Ferretti[24], V.J.G. Feuillard[106], J. Figiel[119], D. Finogeev[64], F.M. Fionda[55,21], G. Fiorenza[34,108], F. Flor[126], A.N. Flores[120], S. Foertsch[73], S. Fokin[90], E. Fragiacomo[61], E. Frajna[146], A. Franco[53], U. Fuchs[34], N. Funicello[29], C. Furget[80], A. Furs[64], J.J. Gaardhøje[91], M. Gagliardi[24], A.M. Gago[113], A. Gal[138], C.D. Galvan[121], P. Ganoti[86], C. Garabatos[109], J.R.A. Garcia[45], E. Garcia-Solis[10], K. Garg[116], C. Gargiulo[34], A. Garibli[89], K. Garner[145], P. Gasik[109], E.F. Gauger[120], A. Gautam[128], M.B. Gay

Ducati[71], M. Germain[116], P. Ghosh[142], S.K. Ghosh[4], M. Giacalone[25], P. Gianotti[52], P. Giubellino[109,60], P. Giubilato[27], A.M.C. Glaenzer[139], P. Glässel[106], D.J.Q. Goh[84], V. Gonzalez[144], L.H. González-Trueba[72], S. Gorbunov[39], M. Gorgon[2], L. Görlich[119], S. Gotovac[35], V. Grabski[72], L.K. Graczykowski[143], L. Greiner[81], A. Grelli[63], C. Grigoras[34], V. Grigoriev[95], S. Grigoryan[76,1], F. Grosa[34,60], J.F. Grosse-Oetringhaus[34], R. Grosso[109], G.G. Guardiano[123], R. Guernane[80], M. Guilbaud[116], K. Gulbrandsen[91], T. Gunji[134], W. Guo[7], A. Gupta[103], R. Gupta[103], S.P. Guzman[45], L. Gyulai[146], M.K. Habib[109], C. Hadjidakis[79], H. Hamagaki[84], M. Hamid[7], R. Hannigan[120], M.R. Haque[143], A. Harlenderova[109], J.W. Harris[147], A. Harton[10], J.A. Hasenbichler[34], H. Hassan[98], D. Hatzifotiadou[54], P. Hauer[43], L.B. Havener[147], S.T. Heckel[107], E. Hellbär[109], H. Helstrup[36], T. Herman[37], E.G. Hernandez[45], G. Herrera Corral[9], F. Herrmann[145], K.F. Hetland[36], H. Hillemanns[34], C. Hills[129], B. Hippolyte[138], B. Hofman[63], B. Hohlweger[92], J. Honermann[145], G.H. Hong[148], D. Horak[37], S. Hornung[109], A. Horzyk[2], R. Hosokawa[15], Y. Hou[7], P. Hristov[34], C. Hughes[132], P. Huhn[69], L.M. Huhta[127], C.V. Hulse[79], T.J. Humanic[99], H. Hushnud[111], L.A. Husova[145], A. Hutson[126], J.P. Iddon[34,129], R. Ilkaev[110], H. Ilyas[14], M. Inaba[135], G.M. Innocenti[34], M. Ippolitov[90], A. Isakov[97], T. Isidori[128], M.S. Islam[111], M. Ivanov[109], V. Ivanov[100], V. Izucheev[93], M. Jablonski[2], B. Jacak[81], N. Jacazio[34], P.M. Jacobs[81], S. Jadlovska[118], J. Jadlovsky[118], S. Jaelani[63], C. Jahnke[123,122], M.J. Jakubowska[143], A. Jalotra[103], M.A. Janik[143], T. Janson[75], M. Jercic[101], O. Jevons[112], A.A.P. Jimenez[70], F. Jonas[98,145], P.G. Jones[112], J.M. Jowett [34,109], J. Jung[69], M. Jung[69], A. Junique[34], A. Jusko[112], J. Kaewjai[117], P. Kalinak[65], A.S. Kalteyer[109], A. Kalweit[34], V. Kaplin[95], A. Karasu Uysal[78], D. Karatovic[101], O. Karavichev[64], T. Karavicheva[64], P. Karczmarczyk[143], E. Karpechev[64], V. Kashyap[88], A. Kazantsev[90], U. Kebschull[75], R. Keidel[47], D.L.D. Keijdener[63], M. Keil[34], B. Ketzer[43], Z. Khabanova[92], A.M. Khan[7], S. Khan[16], A. Khanzadeev[100], Y. Kharlov[93,83], A. Khatun[16], A. Khuntia[119], B. Kileng[36], B. Kim[17,62], C. Kim[17], D.J. Kim[127], E.J. Kim[74], J. Kim[148], J.S. Kim[41], J. Kim[106], J. Kim[74], M. Kim[106], S. Kim[18], T. Kim[148], S. Kirsch[69], I. Kisel[39], S. Kiselev[94], A. Kisiel[143], J.P. Kitowski[2], J.L. Klay[6], J. Klein[34], S. Klein[81], C. Klein-Bösing[145], M. Kleiner[69], T. Klemenz[107], A. Kluge[34], A.G. Knospe[126], C. Kobdaj[117], M.K. Köhler[106], T. Kollegger[109], A. Kondratyev[76], N. Kondratyeva[95], E. Kondratyuk[93], J. Konig[69], S.A. Konigstorfer[107], P.J. Konopka[34], G. Kornakov[143], S.D. Koryciak[2], A. Kotliarov[97], O. Kovalenko[87], V. Kovalenko[114], M. Kowalski[119], I. Králik[65], A. Kravčáková[38], L. Kreis[109], M. Krivda[112,65], F. Krizek[97], K. Krizkova Gajdosova[37], M. Kroesen[106], M. Krüger[69], E. Kryshen[100], M. Krzewicki[39], V. Kučera[34], C. Kuhn[138], P.G. Kuijer[92], T. Kumaoka[135], D. Kumar[142], L. Kumar[102], N. Kumar[102], S. Kundu[34], P. Kurashvili[87], A. Kurepin[64], A.B. Kurepin[64], A. Kuryakin[110], S. Kushpil[97], J. Kvapil[112], M.J. Kweon[62], J.Y. Kwon[62], Y. Kwon[148], S.L. La Pointe[39], P. La Rocca[26], Y.S. Lai[81], A. Lakrathok[117], M. Lamanna[34], R. Langoy[131], K. Lapidus[34], P. Larionov[34,52], E. Laudi[34], L. Lautner[34,107], R. Lavicka[115,37], T. Lazareva[114], R. Lea[141,23,58], J. Lehrbach[39], R.C. Lemmon[96], I. León Monzón[121], E.D. Lesser[19], M. Lettrich[34,107], P. Lévai[146], X. Li[11], X.L. Li[7], J. Lien[131], R. Lietava[112], B. Lim[17], S.H. Lim[17], V. Lindenstruth[39], A. Lindner[48], C. Lippmann[109], A. Liu[19], D.H. Liu[7], J. Liu[129], I.M. Lofnes[21], V. Loginov[95], C. Loizides[98], P. Loncar[35], J.A. Lopez[106], X. Lopez[136], E. López Torres[8], J.R. Luhder[145], M. Lunardon[27], G. Luparello[61], Y.G. Ma[40], A. Maevskaya[64], M. Mager[34], T. Mahmoud[43], A. Maire[138], M. Malaev[100], N.M. Malik[103], Q.W. Malik[20], S.K. Malik[103], L. Malinina[IV,76], D. Mal'Kevich[94], N. Mallick[50], G. Mandaglio[32,56], V. Manko[90], F. Manso[136], V. Manzari[53], Y. Mao[7], G.V. Margagliotti[23], A. Margotti[54], A. Marín[109], C. Markert[120], M. Marquard[69], N.A. Martin[106], P. Martinengo[34], J.L. Martinez[126], M.I. Martínez[45], G. Martínez García[116], S. Masciocchi[109], M. Masera[24], A. Masoni[55], L. Massacrier[79], A. Mastroserio[140,53], A.M. Mathis[107], O. Matonoha[82], P.F.T. Matuoka[122], A. Matyja[119], C. Mayer[119], A.L. Mazuecos[34], F. Mazzaschi[24], M. Mazzilli[34], M.A. Mazzoni[I,59], J.E. Mdhluli[133], A.F. Mechler[69], Y. Melikyan[64], A. Menchaca-Rocha[72], E. Meninno[115,29], A.S. Menon[126], M. Meres[13], S. Mhlanga[125,73], Y. Miake[135], L. Micheletti[60], L.C. Migliorin[137], D.L. Mihaylov[107], K. Mikhaylov[76,94], L.M. Minervini[53], A.N. Mishra[146], D. Miśkowiec[109], A. Modak[4], A.P. Mohanty[63], B. Mohanty[88], M. Mohisin Khan[V,16], M.A. Molander[44], Z. Moravcova[91], C. Mordasini[107], D.A. Moreira De Godoy[145], I. Morozov[64], A. Morsch[34], T. Mrnjavac[34], V. Muccifora[52], E. Mudnic[35], D. Mühlheim[145],

S. Muhuri[142], J.D. Mulligan[81], A. Mulliri[22], M.G. Munhoz[122], R.H. Munzer[69], H. Murakami[134], S. Murray[125], L. Musa[34], J. Musinsky[65], J.W. Myrcha[143], B. Naik[133,49], R. Nair[87], B.K. Nandi[49], R. Nania[54], E. Nappi[53], A.F. Nassirpour[82], A. Nath[106], C. Nattrass[132], A. Neagu[20], L. Nellen[70], S.V. Nesbo[36], G. Neskovic[39], D. Nesterov[114], B.S. Nielsen[91], S. Nikolaev[90], S. Nikulin[90], V. Nikulin[100], F. Noferini[54], S. Noh[12], P. Nomokonov[76], J. Norman[129], N. Novitzky[135], P. Nowakowski[143], A. Nyanin[90], J. Nystrand[21], M. Ogino[84], A. Ohlson[82], V.A. Okorokov[95], L. Oláh[VIII,146], J. Oleniacz[143], A.C. Oliveira Da Silva[132], M.H. Oliver[147], A. Onnerstad[127], C. Oppedisano[60], A. Ortiz Velasquez[70], T. Osako[46], A. Oskarsson[82], J. Otwinowski[119], M. Oya[46], K. Oyama[84], Y. Pachmayer[106], S. Padhan[49], D. Pagano[141,58], G. Paić[70], A. Palasciano[53], J. Pan[144], S. Panebianco[139], J. Park[62], J.E. Parkkila[127], C. Pastore[53], S.P. Pathak[126], R.N. Patra[103,34], B. Paul[22], H. Pei[7], T. Peitzmann[63], X. Peng[7], L.G. Pereira[71], H. Pereira Da Costa[139], D. Peresunko[90,83], G.M. Perez[8], S. Perrin[139], Y. Pestov[5], V. Petráček[37], M. Petrovici[48], R.P. Pezzi[116,71], S. Piano[61], M. Pikna[13], P. Pillot[116], O. Pinazza[54,34], L. Pinsky[126], C. Pinto[26], S. Pisano[52], M. Płoskoń[81], M. Planinic[101], F. Pliquett[69], M.G. Poghosyan[98], B. Polichtchouk[93], S. Politano[30], N. Poljak[101], A. Pop[48], S. Porteboeuf-Houssais[136], J. Porter[81], V. Pozdniakov[76], S.K. Prasad[4], R. Preghenella[54], F. Prino[60], C.A. Pruneau[144], I. Pshenichnov[64], M. Puccio[34], S. Qiu[92], L. Quaglia[24], R.E. Quishpe[126], S. Ragoni[112], A. Rakotozafindrabe[139], L. Ramello[31], F. Rami[138], S.A.R. Ramirez[45], A.G.T. Ramos[33], T.A. Rancien[80], R. Raniwala[104], S. Raniwala[104], S.S. Räsänen[44], R. Rath[50], I. Ravasenga[92], K.F. Read[98,132], A.R. Redelbach[39], K. Redlich[VI,87], A. Rehman[21], P. Reichelt[69], F. Reidt[34], H.A. Reme-ness[36], Z. Rescakova[38], K. Reygers[106], A. Riabov[100], V. Riabov[100], T. Richert[82], M. Richter[20], W. Riegler[34], F. Riggi[26], C. Ristea[68], M. Rodríguez Cahuantzi[45], K. Røed[20], R. Rogalev[93], E. Rogochaya[76], T.S. Rogoschinski[69], D. Rohr[34], D. Röhrich[21], P.F. Rojas[45], P.S. Rokita[143], F. Ronchetti[52], A. Rosano[32,56], E.D. Rosas[70], A. Rossi[57], A. Roy[50], P. Roy[111], S. Roy[49], N. Rubini[25], O.V. Rueda[82], D. Ruggiano[143], R. Rui[23], B. Rumyantsev[76], P.G. Russek[2], R. Russo[92], A. Rustamov[89], E. Ryabinkin[90], Y. Ryabov[100], A. Rybicki[119], H. Rytkonen[127], W. Rzesa[143], O.A.M. Saarimaki[44], R. Sadek[116], S. Sadovsky[93], J. Saetre[21], K. Šafařík[37], S.K. Saha[142], S. Saha[88], B. Sahoo[49], P. Sahoo[49], R. Sahoo[50], S. Sahoo[66], D. Sahu[50], P.K. Sahu[66], J. Saini[142], S. Sakai[135], M.P. Salvan[109], S. Sambyal[103], V. Samsonov[I,100,95], D. Sarkar[144], N. Sarkar[142], P. Sarma[42], V.M. Sarti[107], M.H.P. Sas[147], J. Schambach[98], H.S. Scheid[69], C. Schiaua[48], R. Schicker[106], A. Schmah[106], C. Schmidt[109], H.R. Schmidt[105], M.O. Schmidt[34,106], M. Schmidt[105], N.V. Schmidt[98,69], A.R. Schmier[132], R. Schotter[138], J. Schukraft[34], K. Schwarz[109], K. Schweda[109], G. Scioli[25], E. Scomparin[60], J.E. Seger[15], Y. Sekiguchi[134], D. Sekihata[134], I. Selyuzhenkov[109,95], S. Senyukov[138], J.J. Seo[62], D. Serebryakov[64], L. Šerkšnytė[107], A. Sevcenco[68], I. Sgura[53], T.J. Shaba[73], A. Shabanov[64], A. Shabetai[116], R. Shahoyan[34], W. Shaikh[111], A. Shangaraev[93], A. Sharma[102], H. Sharma[119], M. Sharma[103], N. Sharma[102], S. Sharma[103], U. Sharma[103], O. Sheibani[126], K. Shigaki[46], M. Shimomura[85], S. Shirinkin[94], Q. Shou[40], Y. Sibiriak[90], S. Siddhanta[55], T. Siemiarczuk[87], T.F. Silva[122], D. Silvermyr[82], T. Simantathammakul[117], G. Simonetti[34], B. Singh[107], R. Singh[88], R. Singh[103], R. Singh[50], V.K. Singh[142], V. Singhal[142], T. Sinha[111], B. Sitar[13], M. Sitta[31], T.B. Skaali[20], G. Skorodumovs[106], M. Slupecki[44], N. Smirnov[147], R.J.M. Snellings[63], C. Soncco[113], J. Song[126], A. Songmoolnak[117], F. Soramel[27], S. Sorensen[132], I. Sputowska[119], J. Stachel[106], I. Stan[68], P.J. Steffanic[132], S.F. Stiefelmaier[106], D. Stocco[116], I. Storehaug[20], M.M. Storetvedt[36], P. Stratmann[145], C.P. Stylianidis[92], A.A.P. Suaide[122], C. Suire[79], M. Sukhanov[64], M. Suljic[34], R. Sultanov[94], V. Sumberia[103], S. Sumowidagdo[51], S. Swain[66], A. Szabo[13], I. Szarka[13], U. Tabassam[14], S.F. Taghavi[107], G. Taillepied[136], J. Takahashi[123], G.J. Tambave[21], S. Tang[136,7], Z. Tang[130], J.D. Tapia Takaki[VII,128], M. Tarhini[116], M.G. Tarzila[48], A. Tauro[34], G. Tejeda Muñoz[45], A. Telesca[34], L. Terlizzi[24], C. Terrevoli[126], G. Tersimonov[3], S. Thakur[142], D. Thomas[120], R. Tieulent[137], A. Tikhonov[64], A.R. Timmins[126], M. Tkacik[118], A. Toia[69], N. Topilskaya[64], M. Toppi[52], F. Torales-Acosta[19], T. Tork[79], S.R. Torres[37], A. Trifiró[32,56], S. Tripathy[54,70], T. Tripathy[49], S. Trogolo[34,27], V. Trubnikov[3], W.H. Trzaska[127], T.P. Trzcinski[143], A. Tumkin[110], R. Turrisi[57], T.S. Tveter[20], K. Ullaland[21], A. Uras[137], M. Urioni[58,141], G.L. Usai[22], M. Vala[38], N. Valle[28,58], S. Vallero[60], L.V.R. van Doremalen[63], M. van Leeuwen[92], P. Vande Vyvre[34], D. Varga[146], Z. Varga[146], M. Varga-Kofarago[146], M. Vasileiou[86],

A. Vasiliev[90], O. Vázquez Doce[52,107], V. Vechernin[114], E. Vercellin[24], S. Vergara Limón[45], L. Vermunt[63], R. Vértesi[146], M. Verweij[63], L. Vickovic[35], Z. Vilakazi[133], O. Villalobos Baillie[112], G. Vino[53], A. Vinogradov[90], T. Virgili[29], V. Vislavicius[91], A. Vodopyanov[76], B. Volkel[34,106], M.A. Völkl[106], K. Voloshin[94], S.A. Voloshin[144], G. Volpe[33], B. von Haller[34], I. Vorobyev[107], D. Voscek[118], N. Vozniuk[64], J. Vrláková[38], B. Wagner[21], C. Wang[40], D. Wang[40], M. Weber[115], R.J.G.V. Weelden[92], A. Wegrzynek[34], S.C. Wenzel[34], J.P. Wessels[145], J. Wiechula[69], J. Wikne[20], G. Wilk[87], J. Wilkinson[109], G.A. Willems[145], B. Windelband[106], M. Winn[139], W.E. Witt[132], J.R. Wright[120], W. Wu[40], Y. Wu[130], R. Xu[7], A.K. Yadav[142], S. Yalcin[78], Y. Yamaguchi[46], K. Yamakawa[46], S. Yang[21], S. Yano[46], Z. Yin[7], I.-K. Yoo[17], J.H. Yoon[62], S. Yuan[21], A. Yuncu[106], V. Zaccolo[23], C. Zampolli[34], H.J.C. Zanoli[63], N. Zardoshti[34], A. Zarochentsev[114], P. Závada[67], N. Zaviyalov[110], M. Zhalov[100], B. Zhang[7], S. Zhang[40], X. Zhang[7], Y. Zhang[130], V. Zherebchevskii[114], Y. Zhi[11], N. Zhigareva[94], D. Zhou[7], Y. Zhou[91], J. Zhu[109,7], Y. Zhu[7], G. Zinovjev[3], N. Zurlo[141,58]

Affiliation Notes

[I] Deceased
[II] Also at: Italian National Agency for New Technologies, Energy and Sustainable Economic Development (ENEA), Bologna, Italy
[III] Also at: Dipartimento DET del Politecnico di Torino, Turin, Italy
[IV] Also at: M.V. Lomonosov Moscow State University, D.V. Skobeltsyn Institute of Nuclear, Physics, Moscow, Russia
[V] Also at: Department of Applied Physics, Aligarh Muslim University, Aligarh, India
[VI] Also at: Institute of Theoretical Physics, University of Wroclaw, Poland
[VII] Also at: University of Kansas, Lawrence, Kansas, United States
[VIII] Also at: Earthquake Research Institute, University of Tokyo, Tokyo, Japan

Collaboration Institutes

[1] A.I. Alikhanyan National Science Laboratory (Yerevan Physics Institute) Foundation, Yerevan, Armenia
[2] AGH University of Science and Technology, Cracow, Poland
[3] Bogolyubov Institute for Theoretical Physics, National Academy of Sciences of Ukraine, Kiev, Ukraine
[4] Bose Institute, Department of Physics and Centre for Astroparticle Physics and Space Science (CAPSS), Kolkata, India
[5] Budker Institute for Nuclear Physics, Novosibirsk, Russia
[6] California Polytechnic State University, San Luis Obispo, California, United States
[7] Central China Normal University, Wuhan, China
[8] Centro de Aplicaciones Tecnológicas y Desarrollo Nuclear (CEADEN), Havana, Cuba
[9] Centro de Investigación y de Estudios Avanzados (CINVESTAV), Mexico City and Mérida, Mexico
[10] Chicago State University, Chicago, Illinois, United States
[11] China Institute of Atomic Energy, Beijing, China
[12] Chungbuk National University, Cheongju, Republic of Korea
[13] Comenius University Bratislava, Faculty of Mathematics, Physics and Informatics, Bratislava, Slovakia
[14] COMSATS University Islamabad, Islamabad, Pakistan
[15] Creighton University, Omaha, Nebraska, United States
[16] Department of Physics, Aligarh Muslim University, Aligarh, India

[17] Department of Physics, Pusan National University, Pusan, Republic of Korea
[18] Department of Physics, Sejong University, Seoul, Republic of Korea
[19] Department of Physics, University of California, Berkeley, California, United States
[20] Department of Physics, University of Oslo, Oslo, Norway
[21] Department of Physics and Technology, University of Bergen, Bergen, Norway
[22] Dipartimento di Fisica dell'Università and Sezione INFN, Cagliari, Italy
[23] Dipartimento di Fisica dell'Università and Sezione INFN, Trieste, Italy
[24] Dipartimento di Fisica dell'Università and Sezione INFN, Turin, Italy
[25] Dipartimento di Fisica e Astronomia dell'Università and Sezione INFN, Bologna, Italy
[26] Dipartimento di Fisica e Astronomia dell'Università and Sezione INFN, Catania, Italy
[27] Dipartimento di Fisica e Astronomia dell'Università and Sezione INFN, Padova, Italy
[28] Dipartimento di Fisica e Nucleare e Teorica, Università di Pavia, Pavia, Italy
[29] Dipartimento di Fisica 'E.R. Caianiello' dell'Università and Gruppo Collegato INFN, Salerno, Italy
[30] Dipartimento DISAT del Politecnico and Sezione INFN, Turin, Italy
[31] Dipartimento di Scienze e Innovazione Tecnologica dell'Università del Piemonte Orientale and INFN Sezione di Torino, Alessandria, Italy
[32] Dipartimento di Scienze MIFT, Università di Messina, Messina, Italy
[33] Dipartimento Interateneo di Fisica 'M. Merlin' and Sezione INFN, Bari, Italy
[34] European Organization for Nuclear Research (CERN), Geneva, Switzerland
[35] Faculty of Electrical Engineering, Mechanical Engineering and Naval Architecture, University of Split, Split, Croatia
[36] Faculty of Engineering and Science, Western Norway University of Applied Sciences, Bergen, Norway
[37] Faculty of Nuclear Sciences and Physical Engineering, Czech Technical University in Prague, Prague, Czech Republic
[38] Faculty of Science, P.J. Šafárik University, Košice, Slovakia
[39] Frankfurt Institute for Advanced Studies, Johann Wolfgang Goethe-Universität Frankfurt, Frankfurt, Germany
[40] Fudan University, Shanghai, China
[41] Gangneung-Wonju National University, Gangneung, Republic of Korea
[42] Gauhati University, Department of Physics, Guwahati, India
[43] Helmholtz-Institut für Strahlen- und Kernphysik, Rheinische Friedrich-Wilhelms-Universität Bonn, Bonn, Germany
[44] Helsinki Institute of Physics (HIP), Helsinki, Finland
[45] High Energy Physics Group, Universidad Autónoma de Puebla, Puebla, Mexico
[46] Hiroshima University, Hiroshima, Japan
[47] Hochschule Worms, Zentrum für Technologietransfer und Telekommunikation (ZTT), Worms, Germany
[48] Horia Hulubei National Institute of Physics and Nuclear Engineering, Bucharest, Romania
[49] Indian Institute of Technology Bombay (IIT), Mumbai, India
[50] Indian Institute of Technology Indore, Indore, India
[51] Indonesian Institute of Sciences, Jakarta, Indonesia
[52] INFN, Laboratori Nazionali di Frascati, Frascati, Italy
[53] INFN, Sezione di Bari, Bari, Italy
[54] INFN, Sezione di Bologna, Bologna, Italy
[55] INFN, Sezione di Cagliari, Cagliari, Italy
[56] INFN, Sezione di Catania, Catania, Italy
[57] INFN, Sezione di Padova, Padova, Italy
[58] INFN, Sezione di Pavia, Pavia, Italy
[59] INFN, Sezione di Roma, Rome, Italy

[60] INFN, Sezione di Torino, Turin, Italy
[61] INFN, Sezione di Trieste, Trieste, Italy
[62] Inha University, Incheon, Republic of Korea
[63] Institute for Gravitational and Subatomic Physics (GRASP), Utrecht University/Nikhef, Utrecht, Netherlands
[64] Institute for Nuclear Research, Academy of Sciences, Moscow, Russia
[65] Institute of Experimental Physics, Slovak Academy of Sciences, Košice, Slovakia
[66] Institute of Physics, Homi Bhabha National Institute, Bhubaneswar, India
[67] Institute of Physics of the Czech Academy of Sciences, Prague, Czech Republic
[68] Institute of Space Science (ISS), Bucharest, Romania
[69] Institut für Kernphysik, Johann Wolfgang Goethe-Universität Frankfurt, Frankfurt, Germany
[70] Instituto de Ciencias Nucleares, Universidad Nacional Autónoma de México, Mexico City, Mexico
[71] Instituto de Física, Universidade Federal do Rio Grande do Sul (UFRGS), Porto Alegre, Brazil
[72] Instituto de Física, Universidad Nacional Autónoma de México, Mexico City, Mexico
[73] iThemba LABS, National Research Foundation, Somerset West, South Africa
[74] Jeonbuk National University, Jeonju, Republic of Korea
[75] Johann-Wolfgang-Goethe Universität Frankfurt Institut für Informatik, Fachbereich Informatik und Mathematik, Frankfurt, Germany
[76] Joint Institute for Nuclear Research (JINR), Dubna, Russia
[77] Korea Institute of Science and Technology Information, Daejeon, Republic of Korea
[78] KTO Karatay University, Konya, Turkey
[79] Laboratoire de Physique des 2 Infinis, Irène Joliot-Curie, Orsay, France
[80] Laboratoire de Physique Subatomique et de Cosmologie, Université Grenoble-Alpes, CNRS-IN2P3, Grenoble, France
[81] Lawrence Berkeley National Laboratory, Berkeley, California, United States
[82] Lund University Department of Physics, Division of Particle Physics, Lund, Sweden
[83] Moscow Institute for Physics and Technology, Moscow, Russia
[84] Nagasaki Institute of Applied Science, Nagasaki, Japan
[85] Nara Women's University (NWU), Nara, Japan
[86] National and Kapodistrian University of Athens, School of Science, Department of Physics , Athens, Greece
[87] National Centre for Nuclear Research, Warsaw, Poland
[88] National Institute of Science Education and Research, Homi Bhabha National Institute, Jatni, India
[89] National Nuclear Research Center, Baku, Azerbaijan
[90] National Research Centre Kurchatov Institute, Moscow, Russia
[91] Niels Bohr Institute, University of Copenhagen, Copenhagen, Denmark
[92] Nikhef, National institute for subatomic physics, Amsterdam, Netherlands
[93] NRC Kurchatov Institute IHEP, Protvino, Russia
[94] NRC «Kurchatov»Institute - ITEP, Moscow, Russia
[95] NRNU Moscow Engineering Physics Institute, Moscow, Russia
[96] Nuclear Physics Group, STFC Daresbury Laboratory, Daresbury, United Kingdom
[97] Nuclear Physics Institute of the Czech Academy of Sciences, Řež u Prahy, Czech Republic
[98] Oak Ridge National Laboratory, Oak Ridge, Tennessee, United States
[99] Ohio State University, Columbus, Ohio, United States
[100] Petersburg Nuclear Physics Institute, Gatchina, Russia
[101] Physics department, Faculty of science, University of Zagreb, Zagreb, Croatia
[102] Physics Department, Panjab University, Chandigarh, India
[103] Physics Department, University of Jammu, Jammu, India
[104] Physics Department, University of Rajasthan, Jaipur, India
[105] Physikalisches Institut, Eberhard-Karls-Universität Tübingen, Tübingen, Germany

[106] Physikalisches Institut, Ruprecht-Karls-Universität Heidelberg, Heidelberg, Germany
[107] Physik Department, Technische Universität München, Munich, Germany
[108] Politecnico di Bari and Sezione INFN, Bari, Italy
[109] Research Division and ExtreMe Matter Institute EMMI, GSI Helmholtzzentrum für Schwerionenforschung GmbH, Darmstadt, Germany
[110] Russian Federal Nuclear Center (VNIIEF), Sarov, Russia
[111] Saha Institute of Nuclear Physics, Homi Bhabha National Institute, Kolkata, India
[112] School of Physics and Astronomy, University of Birmingham, Birmingham, United Kingdom
[113] Sección Física, Departamento de Ciencias, Pontificia Universidad Católica del Perú, Lima, Peru
[114] St. Petersburg State University, St. Petersburg, Russia
[115] Stefan Meyer Institut für Subatomare Physik (SMI), Vienna, Austria
[116] SUBATECH, IMT Atlantique, Université de Nantes, CNRS-IN2P3, Nantes, France
[117] Suranaree University of Technology, Nakhon Ratchasima, Thailand
[118] Technical University of Košice, Košice, Slovakia
[119] The Henryk Niewodniczanski Institute of Nuclear Physics, Polish Academy of Sciences, Cracow, Poland
[120] The University of Texas at Austin, Austin, Texas, United States
[121] Universidad Autónoma de Sinaloa, Culiacán, Mexico
[122] Universidade de São Paulo (USP), São Paulo, Brazil
[123] Universidade Estadual de Campinas (UNICAMP), Campinas, Brazil
[124] Universidade Federal do ABC, Santo Andre, Brazil
[125] University of Cape Town, Cape Town, South Africa
[126] University of Houston, Houston, Texas, United States
[127] University of Jyväskylä, Jyväskylä, Finland
[128] University of Kansas, Lawrence, Kansas, United States
[129] University of Liverpool, Liverpool, United Kingdom
[130] University of Science and Technology of China, Hefei, China
[131] University of South-Eastern Norway, Tonsberg, Norway
[132] University of Tennessee, Knoxville, Tennessee, United States
[133] University of the Witwatersrand, Johannesburg, South Africa
[134] University of Tokyo, Tokyo, Japan
[135] University of Tsukuba, Tsukuba, Japan
[136] Université Clermont Auvergne, CNRS/IN2P3, LPC, Clermont-Ferrand, France
[137] Université de Lyon, CNRS/IN2P3, Institut de Physique des 2 Infinis de Lyon, Lyon, France
[138] Université de Strasbourg, CNRS, IPHC UMR 7178, F-67000 Strasbourg, France, Strasbourg, France
[139] Université Paris-Saclay Centre d'Etudes de Saclay (CEA), IRFU, Départment de Physique Nucléaire (DPhN), Saclay, France
[140] Università degli Studi di Foggia, Foggia, Italy
[141] Università di Brescia, Brescia, Italy
[142] Variable Energy Cyclotron Centre, Homi Bhabha National Institute, Kolkata, India
[143] Warsaw University of Technology, Warsaw, Poland
[144] Wayne State University, Detroit, Michigan, United States
[145] Westfälische Wilhelms-Universität Münster, Institut für Kernphysik, Münster, Germany
[146] Wigner Research Centre for Physics, Budapest, Hungary
[147] Yale University, New Haven, Connecticut, United States
[148] Yonsei University, Seoul, Republic of Korea

A Absorbed charge dose

In this section some details on the absorbed charge dose calculation are given. In order to determine the average specific charge dose on the CsI photocathodes, the fraction of the anode current, I_a, that flows through the cathode pad plane is calculated using a simple model. According to the model, I_a consists of two components: I_{cw} which goes through the cathode wires, and I_{cp} collected through the cathode pads. I_{cp} is of interest to calculate the CsI specific charge dose. It is the sum of two components: the first is equal to one-half of the current produced from the charged particle ($I_{MIP/2}$), the second is the full current produced by photoelectrons ($I_{photons}$):

$$I_{cp} = I_{MIP/2} + I_{photons} \tag{A.1}$$

Using the measured average charge for MIPs and for single photoelectron in the MWPC, $\langle Q_{MIP} \rangle$ and $\langle Q_{sphe} \rangle$, we can compute the ratio $r = Q_{sphe}/Q_{MIP}$ and then express I_{cp} as fraction of I_a once the average number of photons per track is calculated. The resulting formula is therefore

$$I_{cp} = f \times I_a \tag{A.2}$$

where f is:

$$f = \frac{0.5 + r \times N_{photons}}{1 + r \times N_{photons}} \tag{A.3}$$

For $N_{photons} = 0$ only one half of the anode current produced by a charged track flows through the cathode pads, whereas for a large number of photons almost all of I_a would flow through the pads.

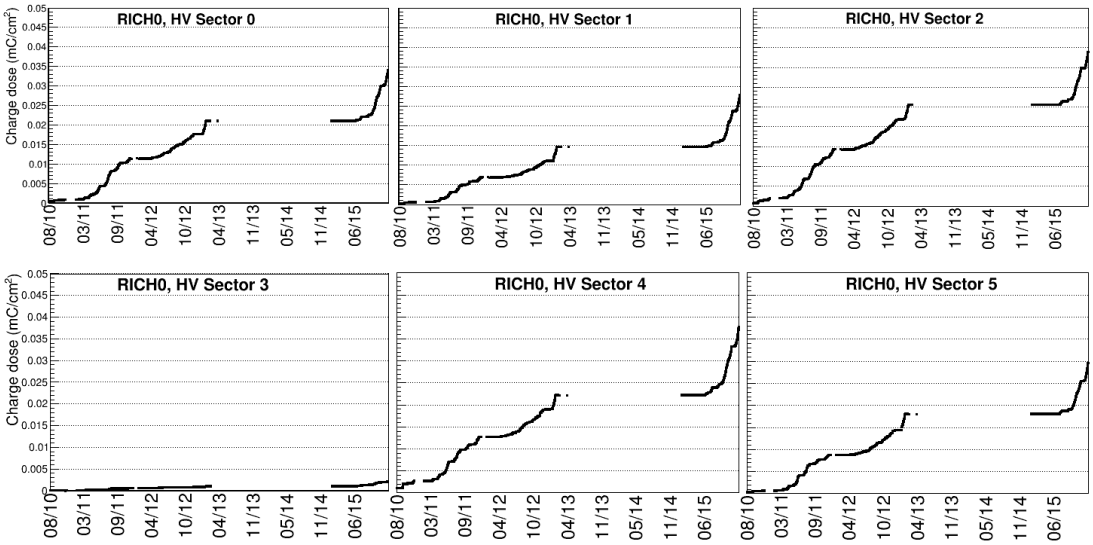

Fig. A.1: Integrated charge dose as a function of time in the various HV sectors of the RICH0. HV sector 3 is a failing one and it is set to a much lower voltage, so the absorbed charge dose is much lower than the other sectors.

In order to choose a realistic value for $N_{photons}$ to be used in eq. (A.3), a set of 23 millions pp collision events recorded in 2010, were analyzed. On average, 2.7 photons per charged track were measured. In this way, the contribution of the photons emitted by the primary avalanche (photon feedback effect [3]) is also taken into account, which for a gas gain of G $\approx 8\times10^4$, is of the order of $N_{ph} \approx 0.03$/avalanche induced by a single electron. With $N_{photons} = 3$ in eq. (A.3), the approximate value of 0.6 for f is obtained. So using $I_{cp} = 0.6\times I_a$, each high voltage sector has produced an average value of specific charge dose of

0.0133 mC/cm^2 on each CsI photocathode. It is calculated integrating a fraction of I_a over the time when the channel voltage is at the operational value of ≈ 2050 and dividing the final value for the PC surface. The HV channels are affected by a pedestal current of 1 nA. For the calculation of the charge dose this value is subtracted from I_a.

In Fig. A.1 the specific charge dose in mC/cm^2 as a function of the time for the RICH0 is shown. Periods with a steeper slope refer to running at a higher collision rate (pp collisions 2011), to increased number of charged particles produced by the beam halo interaction (second half of 2012) or to the p–Pb period (beginning of 2013) where the charged particle multiplicity is higher than in pp. In the 2015 Pb–Pb run, the integrated charge dose of ≈ 0.005 mC/cm^2 for 0.3 nb^{-1} of integrated delivered luminosity can be seen. The bottom-left panel with very low charge dose corresponds to the excluded HV sector where a residual voltage was applied, to reduce the edge effects on the adjacent HV sectors.